Karlsruhe Institute of Technology

Geophysical Institute KIT-Dept. of Physics

ACCURACY OF THE CONVENTIONAL GEOMETRICAL SPREADING CORRECTION FOR SEISMIC WAVES

Master's Thesis of

Armelle Nyamsi Tanly

KIT-Department of Physics
Geophysical Institute (GPI)

Date of submission:

30.09.2024

Reviewer:	Prof. Dr. Thomas Bohlen
Second reviewer:	apl. Prof. Dr. Joachim Ritter

Contents

Chapter 1

Introduction

Seismic waves are affected by several physical parameters of the subsurface, such as wave velocity, density, attenuation, and more. The aim of the inversion in geophysics is always to deduce the material properties of the subsurface from the observed measurement data. Various methods can be used to seek out a subsurface model that can satisfactorily explain the measured data. One of them is the full wave inversion, abbreviated FWI and developed by (Tarantola, 1984).

FWI is an iterative method for determining subsurface parameters based on observed data at the surface and an initial model. Unlike other methods that analyze travel times of individual wave types or limit themselves to reflected or refracted waves, full-waveform inversion utilizes both the amplitude as well as the phase information from all the waves produced to accurately reconstruct the subsurface model. In this method, we do not need to determine single wave types, such as primary (P), secondary(S), or surface waves. This approach has the potential to produce more detailed subsurface information than conventional methods that use travel times or dispersion characteristics (Virieux & Operto, 2009).

The FWI is a nonlinear data fitting procedure designed to obtain estimates of subsurface properties from observed data d_{obs}. The process begins with an initial estimation of the model's parameters m_0. Then the modeled data d_{mod} are predicted by the solution of the wave equation with m_0 (forward modeling). The newly estimated parameters are updated to minimize the mismatch between d_{obs} and d_{mod}. This iterative process is repeated until the fitting error also called the "misfit" between d_{mod} and d_{obs} falls under a previously defined criterion or until the stopping criterion has been reached. That means a proper model to explain the observations is reached (Virieux & Operto, 2009). The result is a high-resolution image of the subsurface.

Solving FWI can be computationally expensive and this is particularly true for 3D scenarios. One of the main drawbacks of implementing a 3D FWI in the time domain is the high computational cost because it is necessary to calculate and save both the forward and backward

fields to calculate the gradient. In other words, the required memory is very expensive. In addition, a large number of operations are required, which results in a very long execution time (Plessix, 2006). To reduce the long computation time, it is preferable to apply the 2-D FWI. With the 2D approach, it is also possible to perform many repetitions on medium-sized computers. While 2-D adjoint waveform inversion inherently uses line sources in 3-D space, the 3-D approach uses a point source.

How the wave propagates in a medium depends on the source of excitation. If the wave is generated by a point source, the wave will propagate in all directions from a point source, its shape is spherically symmetric and the amplitude decreases with the distance from the source (3-D geometrical spreading). This wave is called a spherical wave since its crests are spheres centered in the source. If the source is a line, the resulting wave is cylindrical (2D geometrical spreading). Wave excited by a point source differ in geometrical spreading, i.e. amplitude decay and phase delay of $\frac{\pi}{4}$ from waves excited by a line source (Schäfer et al., 2012). The recorded data in the field are generated by point sources (hammer blow or an explosion) and produce wavefields with 3D spreading. We do not take into account the simulation of a line source in the field study. This would require a large number of dense shots perpendicular to the seismic profile to achieve superior results to the approach with point sources. The effort required for such an approach is too important to be acceptable in practice (Schäfer et al., 2011) .

With the purpose to apply a 2-D FWI of recorded data, we have to handle with the different geometrical spreading of point and line sources, because a 2-D synthetic forward modeling code uses line sources and produces wavefields with 2-D spreading. When we carry out 2-D FWI with 3D data acquired in a field, critical problems happen in FWI, because 2-D and 3-D wave equations have different Green's functions (Taekhyun et al., 2016). To overcome the problem, a correction of the different geometrical spreading, due to unequal decaying in amplitude and a certain shift in phase, is consequently required. Recorded data have to be transformed to corresponding waveforms as would be generated by line sources (Schäfer et al., 2011). There are different numerical transformations that we can apply to point source wavefields to simulate line source wavefields. To correct the effect of the geometrical spreading, I will discuss two different 3-D/2-D transformation techniques. One of them is derived from the ratio of the Fourier coefficients of the 2-D and 3-D Green's functions for homogeneous fullspace, which are defined in ((Morse & Feshbach, 1953) ,eq. 7.2.18,eq. 7.2.19). With this transformation, we should obtain equivalent line-source seismograms from observed measurement data. Previous work on the subject, drawn from the literature, shows that the accuracy of correction has so far only been studied systematically in part. Therefore, this will be done in this work using simple models. In order to make quantitative statements, the seismograms should also be compared with analytical solutions as far as available. The other transformation technique is the source time function inversion. The most important differences between the recorded data and the synthetic data are due

to the differences between the true subsurface model and the two-dimensional subsurface model which is used in the simulations. In addition, the differences are due to differences in the time function of the source. As an essential part of the FWI workflow, the source signal must be inverted together with the earth model given here by the Greens function. A Wiener filter is usually used for this source time function inversion. This linear filter in the frequency domain called source wavelet correction filter should minimize the difference between the true source signal and the initial synthetic source so that the field data (point-source seismograms) are transformed into equivalent line-source seismograms.
It is important to mention that in this work, no FWI reconstructions are performed, but only the accuracy of the different 3-D/2-D transformations is evaluated by comparing waveforms.

This thesis is organized as follows.

After the introduction, **chapter 2** describes the essential theory needed to understand the methodological approach of this work. First, I gave a mathematical definition of point and line sources, then I derived the acoustic wave equation and from this equation, I derived the Green's functions in 2D and 3D, which are useful for the derivation of the geometry spreading correction filter, then I made different practical implementation of the amplitude correction depending on the travel path of the waves. Afterward, I focused on the derivation of the source wavelet correction filter.

Chapter 3 shows the systematic study of the applicability of the geometrical spreading transformation. Two models will be taken into account: A homogeneous full-pace model and a reflector model composed of two layers. For each model, 2-D and 3-D synthetic data will be generated using two different methods, namely the analytical solutions and the numerical solutions (Finite Difference(FD) method). Different transformations (reflected-wave , direct-waves and exact transformation) are applied on 3-D generated seismograms (point-source seismograms) with the aim to obtain the 2D generated seismograms (line-source seismograms).

In **chapter 4** the source time inversion will be used to solve the problem of the geometrical spreading. The wavelet filter is performed for the same models and data computed in chapter 3.

How source signal inversion behaves in relation to the transformations performed in Chapter 3, and whether source time function inversion alone is sufficient, will be the focus of our attention in **chapter 5**.

Finally, **Chapter 6** summarizes the main results of the work.

Chapter 2

Theory

This chapter will describe the theoretical background on which this work is based. It is divided into five main sections. I begin with a mathematical definition of point and line sources in Section 2.1. After that, I describe in section 2.2 the geometrical spreading for point and line sources. Section 2.3 provides an overview of the wave equation for an acoustic medium. Section 2.4 focuses on the derivation of Green's functions for the acoustic wave equation in one dimension (1-D), two dimensions (2-D), and three dimensions (3-D) of space. In Section 2.5, I derive the geometrical spreading correction filter for 2-D and 3-D. Finally, section 2.6 deals with the derivation of the source-wavelet correction filter.

2.1 Point source and line source

2.1.1 Definition of point source

The following formula gives the linear, viscoelastic vector differential equation

$$\hat{L}_{kl}(\vec{x})u_l(\vec{x},t) = f_k(\vec{x},t), \tag{2.1}$$

where $\hat{L}_{kl}(x)$ is the vector differential operator (Aki & Richards, 2002) containing the mass density and elastic parameters. These parameters depend on the location. u_l is the l-component of the particle displacement vector and f_k the k-component of an external force density (Forbriger et al., 2014). The source that excites the seismic waves is introduced by a point source

$$f_p(\vec{x},t;\vec{x_s}) = F(t)\delta_x(\vec{x}-\vec{x_s}) \tag{2.2}$$

at the location $\vec{x}_s$, where $\delta_x(\vec{x})$=$\delta_x(x)\delta_x(y)\delta_x(z)$ is Dirac's delta function and $\vec{F}(t)$ is the applied force vector which changes with respect to time. A general approach to express the

solution of equation (2.1) is the Green's dyadic $G(\vec{x}, t; \vec{x'}, t')$. It is the solution to

$$\hat{L}(\vec{x})G(\vec{x}, t; \vec{x'}, t') = \underline{\mathbf{1}}\delta_x(\vec{x} - \vec{x'})\delta_t(t - t'), \tag{2.3}$$

where $\underline{\mathbf{1}}$ is the unit tensor. $\delta_x(\vec{x})$ and $\delta_t(t)$ are Dirac's delta functions with physical units of $\frac{1}{m^3}$ and $\frac{1}{s}$, respectively (Forbriger et al., 2014). The particle displacement and solution of Equation (2.1) for an arbitrary force density is

$$u(\vec{x}, t) = \int_{-\infty}^{+\infty} \iiint_V G(\vec{x}, t; \vec{x'}, t') f(\vec{x'}, t') d^3\vec{x'} dt', \tag{2.4}$$

The integration limits have the units of time t and spatial coordinates x, y, and z, respectively. In the case of a point source as defined in equation 2.2 the displacement field is

$$u_P(\vec{x}, t, \vec{x_s}) = \int_{-\infty}^{+\infty} \iiint_V G(\vec{x}, t; \vec{x'}, t') \vec{F}(t) \delta_x(\vec{x'} - \vec{x_s}) d^3\vec{x'} dt', \tag{2.5}$$

$$= \int_{-\infty}^{+\infty} G(\vec{x}, t; \vec{x_s}, t') \vec{F}(t') dt', \tag{2.6}$$

and since the material properties do not change with time

$$= \int_{-\infty}^{+\infty} G(\vec{x}, t - t'; \vec{x_s}, 0) \vec{F}(t') dt', \tag{2.7}$$

which is the convolution of Green's function with the force which depends on the time.

2.1.2 Definition of line source

A line source is defined as a force density that extends to infinity in the y-direction so that

$$f_l(x, y, z, t; x_s, z_s) = F(t) C \delta_x(x - x_s) \delta_x(z - z_s) \tag{2.8}$$

where $C = 1m^{-1}$. This corresponds to a superposition of an infinite number of point sources along the y-axis (Forbriger et al., 2014). The particle displacement generated by this source is

$$u_L(x, y, z, t; x_s, z_s) = \int_{-\infty}^{+\infty} \int_{-\infty}^{+\infty} \int_{-\infty}^{+\infty} \int_{-\infty}^{+\infty} G(x, y, z, t; x', y', z', t') \\ F(t) C \delta_x(x' - x_s) \delta_x(z' - z_s) dx' dy' dz' dt, \tag{2.9}$$

$$= \int_{-\infty}^{+\infty} \int_{-\infty}^{+\infty} G(x, y, z, t - t'; x_s, y', z_s, 0) F(t') C dy' dt'. \tag{2.10}$$

The displacement field generated by the line source can be expressed in terms of the displacement field which is generated by the point source. It is

$$u_L(x, y, z, t; x_s, z_s) = \int_{-\infty}^{+\infty} u_p(x, y, z, t; x_s, y', z_s) C dy', \tag{2.11}$$

which corresponds to a superposition of displacement fields generated by point sources along a line in the y direction (Forbriger et al., 2014).

2.2 Geometrical spreading

We understand the geometrical spreading as the decrease in amplitude of the seismic wave due to its geometric spreading in the subsurface. As the wavefront moves away from the source, the energy originally released in the seismic wave spreads over an increasing surface and consequently the amplitude of the wave decreases with distance. In this part, I will discuss two cases: 2D and 3D geometrical spreading for a line source and point source, respectively.

2.2.1 geometrical spreading for point source

Figure 2.2 shows a point source located at the origin of the 3-D Cartesian coordinate system. In a homogeneous 3 -D space the wave's energy spreads on the surface of an expanding sphere centered on the origin. This means the wavefronts are spherical. Consequently, the recorded amplitude by a receiver at a distance r_0 decays with r_0^{-1} (Forbriger et al., 2014).

2.2.2 geometrical spreading for line source

The line source can be interpreted as a superposition of a continuous arrangement of point sources along the y-axis, which emit an impulsive signal at $t = 0$ (see figure 2.1). The receiver located on the x-axis at the source-receiver distance r_0 will first record the wave generated by the point source at the origin. Because the offset $r_0 = \sqrt{x^2 + y^2}$ increases with y, contributions from point sources located at locations where $|y|$ is larger will arrive later and with decreasing amplitude. The propagation of seismic energy occurs on the surface of an expandable cylinder centered on the y-axis. In other words, the wavefronts emitted by a line source are cylindrical. Consequently, the amplitudes in the far-field will decay with $\sqrt{r_0^{-1}}$ (Forbriger et al., 2014).

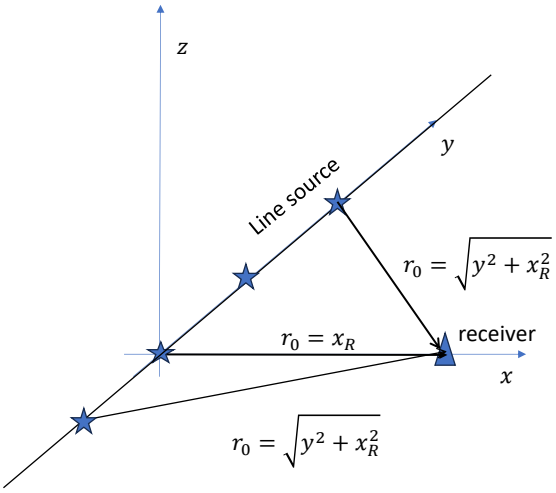

(a) Line source sketched along the y-axis of the 3 -D Cartesian coordinate system. The triangle marks a receiver's location at $x = x_R$ and $y = z = 0$.

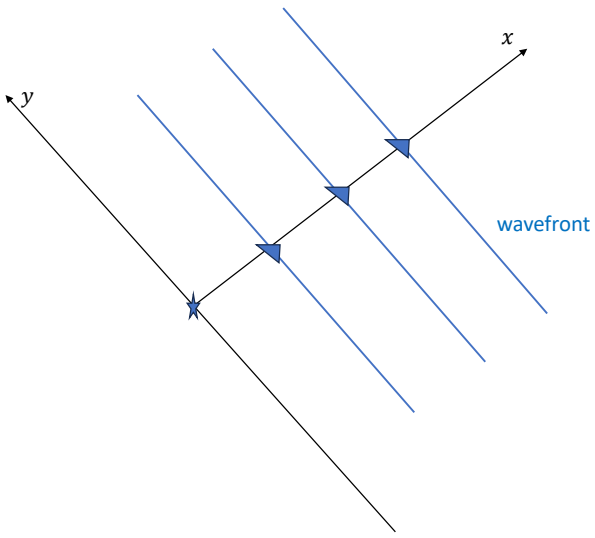

(b) Wavefront emitted by a line source.

Figure 2.1: Description of geometrical spreading in a 2D simulation.

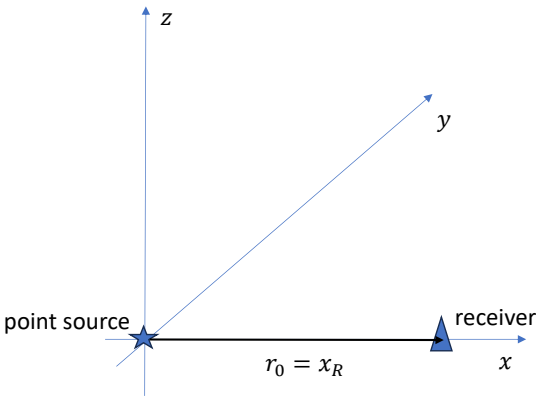

(a) Point source represented by a star and sketched at the origin of the 3 -D Cartesian coordinate system. The triangle marks the location of a receiver at $x = x_R$ and $y = z = 0$

.

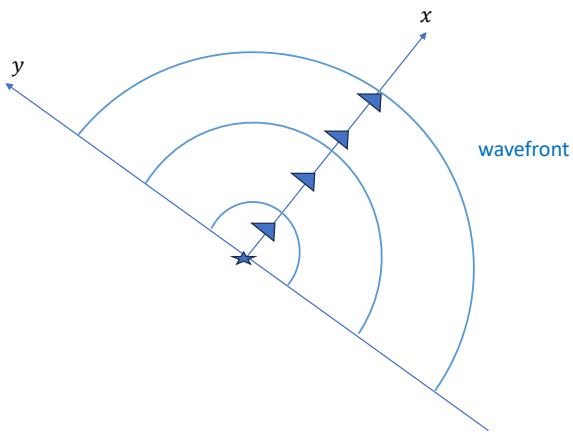

(b) Wavefront emitted by a point source.

Figure 2.2: Description of geometrical spreading in a 3D simulation.

2.3 Seismic wave propagation in acoustic media

If deformations exist in a body from an undisturbed configuration, combined with the change in length of distances, stresses occur in it. This means, at each point of the body there is a functional relationship between the components of the stress tensor σ and those of the deformation tensor ϵ. In the case of infinitesimal deformations, the linear elasticity theory is valid and we assume a linear relation between stress and deformation (strain) tensor, also known as Hooke's law (Lay & Wallace, 1995) given by

$$\sigma_{ij} = C_{ijkl}\epsilon_{kl} \ , \qquad i,j,k,l \in [1,3] \tag{2.12}$$

where σ_{ij} represents the stress tensor, C_{ijkl} the elasticity (or stiffness) tensor, which contains the elasticity moduli (Lay & Wallace, 1995) and ϵ_{kl} the strain tensor, given by

$$\epsilon_{kl} = \frac{1}{2}\left(\frac{\partial u_k}{\partial x_l} + \frac{\partial u_l}{\partial x_k}\right) \qquad k,l \in [1,3] \ . \tag{2.13}$$

The parameters u_k and u_l represent respectively the displacement of a particle in the direction of the l-th and k-th dimension, of a Cartesian coordinate system. C_{ijkl} is a fourth order tensor with 81 $(= 9 \times 9)$ components. Due to the symmetry properties of the stress tensor $\sigma_{ij} = \sigma_{ji}$ and the deformation tensor $\epsilon_{kl} = \epsilon_{lk}$ only 36 $(= 6 \times 6)$ components are independent. Moreover the number of elasticity moduli can be reduced further to 21 due to the conservation of the volume density of elastic energy (Müller, 2007). This number is further reduced in the case of a special form of anisotropy and in particular in the case of isotropy. Assuming an isotropic elastic media, the number further decreases to two independent parameters, known as the Lamé (or elastic) parameters λ and μ. the stress-strain relation for isotropic media is now written as

$$\sigma_{ij} = \lambda\theta\delta_{ij} + 2\mu\epsilon_{ij}. \tag{2.14}$$

μ is also referred to as the shear modulus, its combination with λ yields the P-wave modulus $\pi = \lambda + 2\mu$. The parameter $\theta = \epsilon_{11} + \epsilon_{22} + \epsilon_{33}$ is the cubic dilatation, which is the trace of the strain tensor and the parameter

$$\delta_{ij} = \begin{cases} 1 & \text{if } i = j \text{ and} \\ 0 & \text{otherwise} \end{cases}$$

is the so-called Kronecker symbol.

To describe wave propagation, not only the stress-strain relation is needed but also the equa-

tion of motion, which can be derived from Newton's second law:

$$\rho \frac{\partial v_i}{\partial t} = \frac{\partial \sigma_{ij}}{\partial x_j} + f_i \, . \tag{2.15}$$

This equation states that the momentum of the medium, the product of density ρ and the derivative of displacement velocity $v_i = \frac{\partial u_i}{\partial t}$, i.e., acceleration, can be modified by surface forces, described by the stress tensor p_{ij} or body forces f_i. The equation of motion is valid for any volume, independently if it is filled with a liquid, a gas, or a rock (Müller, 2007). Taking the time derivative of equation 2.14, leads to the equation for the velocity-stress formulation of wave propagation:

$$\frac{\partial \sigma_{ij}}{\partial t} = \lambda \frac{\partial \theta}{\partial t} \delta_{ij} + 2\mu \, \frac{\partial \epsilon_{ij}}{\partial t}. \tag{2.16}$$

With equations 2.15 and 2.16 elastic wave propagation is expressed.

For the acoustic case, which corresponds to wave propagation in fluids, two simplifications can be used. The second Lamé parameter (shear modulus) is zero ($\mu = 0$) in fluids; as a consequence, the velocity of the shear waves (S-waves), which is expressed by $V_s = \frac{\mu}{\rho}$, also vanishes. Only pressure waves are propagating and no shear waves exist. The stress-strain relation given in equation 2.14 can be rewritten as

$$\sigma_{ij} = \lambda \theta \delta_{ij}. \tag{2.17}$$

The stress tensor σ_{ij} is therefore reduced to its diagonal elements, which all take the value $\epsilon_{kk} = \frac{\partial u_k}{\partial x_k}$. The absence of shear stresses in fluids causes hydrostatic stress or pressure p defined as the mean of normal stress σ_{ii}, so $-p = \frac{1}{3}\sigma_{ii}$, equation 2.17 becomes then

$$\sigma_{ij} = \lambda \theta \delta_{ij} = \lambda \delta_{ij} \epsilon_{kk} = \lambda \delta_{ij} \frac{\partial u_k}{\partial x_k} = \begin{pmatrix} -p & 0 & 0 \\ 0 & -p & 0 \\ 0 & 0 & -p \end{pmatrix} = -p \delta_{ij}. \tag{2.18}$$

By inserting equation 2.18 into equations 2.15 and 2.16, and assuming that there are no external forces, we can simplify the equation of motion:

$$\rho \left(\frac{\partial^2 u_i}{\partial t^2} \right) = \rho \left(\frac{\partial v_i}{\partial t} \right) = \frac{\partial p}{\partial x_i} \qquad i \in [1, 3] \, . \tag{2.19}$$

With equation 2.16 the time derivative of the pressure is

$$\frac{\partial p}{\partial t} = -\lambda \frac{\partial \epsilon_{kk}}{\partial t} = -\lambda \frac{\partial}{\partial t} \left(\frac{\partial u_k}{\partial x_k} \right) = -\lambda \frac{\partial v_k}{\partial x_k} \qquad k \in [1, 3] \, . \tag{2.20}$$

Equation 2.20 is the first-order acoustic wave equation. To obtain a second-order partial

differential equation, we differentiate once more equation 2.20 concerning time, leading to equation 2.21:

$$-\frac{\partial^2 p}{\partial t^2} = \lambda \frac{\partial}{\partial x_k}\left(\frac{\partial v_k}{\partial t}\right) = \lambda\left(\frac{\partial}{\partial x_1}\frac{\partial v_1}{\partial t} + \frac{\partial}{\partial x_2}\frac{\partial v_2}{\partial t} + \frac{\partial}{\partial x_3}\frac{\partial v_3}{\partial t}\right) \tag{2.21}$$

and then we insert equation 2.19

$$-\frac{\partial^2 p}{\partial t^2} = -\lambda\left(\frac{\partial}{\partial x_1}\left(\frac{1}{\rho}\frac{\partial p}{\partial x_1}\right) + \frac{\partial}{\partial x_1}\left(\frac{1}{\rho}\frac{\partial p}{\partial x_1}\right) + \frac{\partial}{\partial x_1}\left(\frac{1}{\rho}\frac{\partial p}{\partial x_1}\right)\right) \tag{2.22}$$

This equation can also be written as:

$$\frac{\partial^2 p}{\partial t^2} = \lambda \sum_{i=1}^{3} \frac{\partial}{\partial x_i}\left(\frac{1}{\rho}\frac{\partial p}{\partial x_i}\right) \tag{2.23}$$

Assuming a constant mass density ρ, we obtain the well-known form of the acoustic wave equation

$$\frac{\partial^2 p}{\partial t^2} = \frac{\lambda}{\rho}\nabla^2 p = c^2 \nabla^2 p \tag{2.24}$$

with the acoutic wave velocity $c = \sqrt{\frac{\lambda}{\rho}}$ and a constant density ρ =const. This can also be written as

$$\left(\frac{1}{c^2}\frac{\partial}{\partial t^2} - \nabla^2\right) p = 0 \tag{2.25}$$

where ∇ denotes the Nabla operator and its square ∇^2 is the Lapace-Operator, which can also be written as symbol Δ (Müller, 2007).

2.4 Green's function (GF) for the acoustic wave equation

After deriving the wave equation, we can now look at Green's functions. Green's functions can be interpreted as the impulse response of the wave equation, which means that it is the solution of the equation with a delta function as source function. To derive the GF I will consider the acoustic wave equation without neglecting the external forces:

$$\left[\frac{1}{c^2}\frac{\partial}{\partial t^2} - \nabla^2\right] p(\vec{x}, \vec{x_s}, t) = f(\vec{x_s}, t). \tag{2.26}$$

In the field, we can record pressure change as a function of time t and distance x to the source. Here, p is the pressure, c the acoustic wave velocity, $\vec{x_s}$ the source location, and f the source function. Because the Green's function is the solution of this equation with a delta

function as source function, it should satisfy the equation below:

$$\left[\frac{1}{c^2}\frac{\partial}{\partial t^2} - \nabla^2\right] G(\vec{x}, \vec{x_s}, t) = \delta(\vec{x} - \vec{x_s}, t)\delta t \tag{2.27}$$

The source function describes a delta-impulse at the location $x = x_s$ and at the time $t = 0$. Consequently, the Green's function depends on the receiver position x, the source position x_s, and the time t. If we know the Green's function, we can calculate the pressure field for any other source function by convolving the Green's function with the source function.

$$p(\vec{x}, \vec{x_s}, t) = G(\vec{x}, \vec{x}_s, t) * f(\vec{x}_s, t), \tag{2.28}$$

where the asterisk $*$ indicates convolution. In the following I will discuss the Green's functions for homogenous media with a constant velocity c = const in the frequency domain. I therefore have to apply a Fourier transformation (FT) of equation 2.27. In this study, the definition of the Fourier transformation is:

$$u(t) = \frac{1}{2\pi}\int_{-\infty}^{+\infty} \tilde{u}(\omega)e^{i\omega t}\, d\omega \tag{2.29}$$

$$\tilde{u}(\omega) = \int_{-\infty}^{+\infty} u(t)e^{-i\omega t}\, dt \tag{2.30}$$

where $u(t)$ is a function of time and $\tilde{u}(\omega)$ is its Fourier transform. In the frequency domain, equation 2.27 becomes:

$$\left[k^2 + \Delta\right] \tilde{G}(\vec{x}, \vec{x_s}, \omega) = -4\pi\delta(\vec{x} - \vec{x_s}) \tag{2.31}$$

this equation is called the Helmholtz equation where $k = w/c$ is the wave number for angular frequency w and wave velocity c. Assuming a constant velocity c, the following solutions of the Helmholtz equation in the region where the signature shape does not change significantly with distance (far field), can be derived. For details, I referred to (Morse & Feshbach, 1953). In three dimensions of space the Green's function is given ((Morse & Feshbach, 1953), eq. 7.2.17) and reads

$$\tilde{G}^{3D}(\vec{x}; \vec{x_s}, \omega) = g^{3D}(r_{xyz}) = \frac{e^{-ikr_{xyz}}}{r_{xyz}}, \tag{2.32}$$

with $\vec{x} = (x, y, z)$, $\vec{x_s} = (x_s, y_s, z_s)$ and $r_{xyz} = \sqrt{(x - x_s)^2 + (y - y_s)^2 + (z - z_s)^2}$.

In the case of the two dimensions, the correct Green's function is given in (Morse & Feshbach 1953, eq. 7.2.18)

$$\tilde{G}^{2D}(\vec{x}, \vec{x_s}, \omega) = g^{2D}(r_{xz}) = i\pi H_0^{(1)}(kr_{xz}) \tag{2.33}$$

with $\vec{x} = (x, z)$, $\vec{x_s} = (x_s, , z_s)$ and $r_{xz} = \sqrt{(x - x_s)^2 + (z - z_s)^2}$. $H_0^{(1)}$ is the Hankel

function of the first kind and order zero. The far-field approximation is

$$\lim_{r_{xz}\to\infty} g^{2D}(r_{xz}) = \sqrt{\frac{2\pi}{kr_{xz}}}e^{-ikr_{xz}}e^{i\pi/4} = \sqrt{\frac{2\pi}{kr_{xz}}}e^{-i_{(kr_{xz}+\pi/4)}} \tag{2.34}$$

$$\tilde{G}^{2D}(\vec{x};\vec{x_s},\omega) = \sqrt{\frac{2\pi}{kr_{xz}}}e^{-i_{(kr_{xz}+\pi/4)}}. \tag{2.35}$$

For completeness, the Green's function for one dimension is also given (Morse & Feshbach 1953, eq. 7.2.19) and reads

$$\tilde{G}^{1D}(\vec{x},\vec{x_s},\omega) = g^{1D}(r_x) = \frac{2\pi i}{k}e^{-ikr_x}, \tag{2.36}$$

with $r_x = |x - x_s|$. In (Forbriger et al., 2014), it is demonstrated that if we apply the definition of the line source in equation (2.11) to $\tilde{G}^{3D}$ we reproduce $\tilde{G}^{2D}$. Without loss of generality, The source coordinates are set to zero ($x_s = y_s = z_s = 0$). Applying integration along y like in equation (2.11) and after some lines of calculus 2-D green's function is obtained

$$\int_{-\infty}^{+\infty} g^{3D}(r_{xyz})Cdy = \int_{-\infty}^{+\infty} \frac{e^{-ik\sqrt{x^2+y^2+z^2}}}{\sqrt{x^2+y^2+z^2}}Cdy, = iC\pi H_0^{(1)}(k\sqrt{x^2+z2} = g^{2D}(r_{xz}). \tag{2.37}$$

It is important to note that in (Morse & Feshbach, 1953) there is no minus sign (-) in the exponential part of the Green's functions because another definition of the Fourier transformation was used:

$$u(t) = \frac{1}{2\pi}\int_{-\infty}^{+\infty} \tilde{u}(\omega)e^{-i\omega t}\,d\omega \tag{2.38}$$

$$\tilde{u}(\omega) = \int_{-\infty}^{+\infty} u(t)e^{i\omega t}\,dt \tag{2.39}$$

2.5 Geometrical-spreading correction filter

Knowing the Green's function in the frequency domain, I formulated a geometrical spreading correction filter F. While waves excited by point sources are represented by a convolution of the source function $f(t)$ with the Green's function G^{3D}, waves generated by line sources in 3-D full space are expressed by a convolution of $f(t)$ with G^{2D} in the time domain. From the Fourier transform $\tilde{u_P}$ of a wave excited by a point source, we can deduce the corresponding wave $\tilde{u_L}$ produced by an equivalent line source by multiplication with $\frac{\tilde{G^{2D}}}{\tilde{G^{3D}}}$ (Forbriger et al., 2014). Consequently, for a source located at the origin of the coordinate system, the waves

generated by the line source in the far-field were as follows

$$\lim_{r_{xz}\to\infty} \tilde{u}_L(r_{xz},\omega) = F(r_{xz},k)\tilde{u}_P(r_{xyz}=r_{xz},\omega) \tag{2.40}$$

with

$$F(r_{xz},k) = \lim_{r_{xz}\to\infty} \frac{g^{2D}\left(r_{xz}\right)}{g^{3D}\left(r_{xz}\right)} = \frac{\sqrt{\frac{2\pi}{kr_{xz}}}e^{-i(kr_{xz}+\pi/4)}}{\frac{e^{-ikr_{xz}}}{r_{xz}}} = \sqrt{\frac{2\pi r_{xz}}{k}}e^{-i\pi/4}. \tag{2.41}$$

The correction filter can be simply expressed like:

$$F(r,k) = \sqrt{\frac{2\pi r}{k}}e^{-i\pi/4} \tag{2.42}$$

(Forbriger et al., 2014). The filter $F(r,k)$ effects a phase shift of $\pi/4$ to the waves and a spreading correction to the amplitudes, depending on the travel path r and wavenumber k. The wavenumber can be substituted in the equation with $k = w/c$ to have the velocity c in the correction filter, which is a more useful quantity when talking about wave propagation. So the above equation becomes

$$F(r,\omega) = \sqrt{\frac{2\pi r}{k}}e^{-i\pi/4} = \sqrt{\frac{2\pi rc}{\omega}}e^{-i\pi/4} = \underbrace{\sqrt{2rc}}_{F_{amp}}\underbrace{\sqrt{\frac{\pi}{\omega}}e^{-i\pi/4}}_{\tilde{F}_{\sqrt{t^{-1}}}} \tag{2.43}$$

$\tilde{F}_{\sqrt{t^{-1}}}$ is the Fourier transform of the function $\sqrt{t^{-1}}$ (Forbriger et al., 2014). I noticed that the correction filter $F(r,w)$ could be divided into two factors. The first factor $F_{amp} = \sqrt{2rc}$ is defined as the $amplitude\ correction$. It depends on the travel path r as well as on the velocity c. In field observations, these parameters are in general unknown. We can also notice that the amplitude factor does not depend on frequency and therefore can be applied equally in the Fourier or time domain.
The second factor

$$\tilde{F}_{\sqrt{t^{-1}}}(\omega) = \sqrt{\frac{\pi}{\omega}}e^{-i\pi/4} = \sqrt{\frac{\pi}{2|\omega|}}(1+\mathrm{isgn}(\omega)) \tag{2.44}$$

defines the $phase\ correction$, which is independent of the propagation distance and the wave velocity c. It applies to every constituent of the wavefield in the same way. An application can be done in the Fourier domain or by convolution with

$$F_{\sqrt{t^{-1}}}(t) = \begin{cases} \frac{1}{\sqrt{t}} & \text{if t} \geq 0 \text{ and} \\ 0 & \text{otherwise} \end{cases} \tag{2.45}$$

in the time domain (Forbriger et al., 2014).

2.5.1 Amplitude correction

The spreading amplitude correction $F_{amp} = \sqrt{2rc}$ depends on the propagating distance r. The relation $r = |\vec{x} - \vec{x_s}|$, which described the offset (distance between source and receiver) is only applicable for a homogeneous medium, where no reflections can occur, which means that the velocity in the medium is constant. In field observations we have in general a heterogenous medium. Different kinds of waves can be recorded in the field, for instance: reflected waves, direct waves, refracted waves, surface waves, and so forth. For each of those waves, the travel path is different. This leads to different practical implementations of the amplitude correction depending on the travel path of the waves (Forbriger et al., 2014).
Figure 2.3 shows the travel path of a direct and a reflected wave. I examined three different cases, (a) direct-wave transformation, (b) reflected-wave transformation, and (c) exact transformation without approximation for waves propagating in a homogeneous medium.

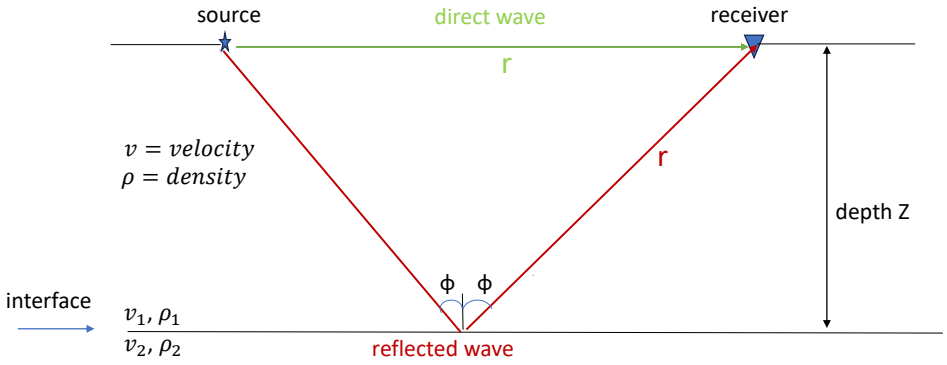

Figure 2.3: Travel path of a direct wave and a reflected in green and red line, respectively

a) Reflected-wave transformation

As mentioned above, the spreading correction filter depends on two factors, the phase factor and the amplitude factor. The amplitude factor given by $F_{amp} = \sqrt{2rc}$ depends on the propagation distance and the velocity. In the seismic reflection method, the waves travel downward initially and are reflected at some point back to the surface. If we know the depth of the reflector and also know the offset (source-receiver distance), we can simply calculate the propagation distance using the Pythagorean theorem

$$d = \sqrt{z^2 + \left(\frac{x}{2}\right)^2} \tag{2.46}$$

$$r = 2d \tag{2.47}$$

where z is the depth to the reflector and x the offset, d the one-way travel path and r the propagation distance.

Unfortunately, in seismic imaging applications we assume that the seismic wave velocity in the rock is known approximately, while the propagation distance r, which depends on the ray path and the location of reflection in particular, is unknown because we do not know the depth to the reflector. However, the knowledge of the travel-time to the receiver and the velocity of waves in the medium enable us to reconstruct the paths of seismic waves. The travel-time t from the surface to the reflector and back is called the two-way time and is given by the formula

$$t = \frac{2d}{c} = \frac{r}{c}. \tag{2.48}$$

With an average velocity c and the recorded time t, the travel path is

$$r = ct. \tag{2.49}$$

Substituting r in the amplitude correction expression to eliminate it, the amplitude factor becomes

$$F_{amp_{refl}}(t) = \sqrt{2rc} = c\sqrt{2t}. \tag{2.50}$$

$F_{Amp_{refl}}$ represents the amplitude correction factor for reflected waves. It is therefore proportional to the square root of the travel-time, which simplifies the correction. After replacing this amplitude factor $F_{amp_{refl}}$ in the correction filter expressed in equation 2.42, it becomes

$$F_{reflected} = \underbrace{c\sqrt{2t}}_{F_{amp_{refl}}} \underbrace{\sqrt{\frac{\pi}{\omega}} e^{i\pi/4}}_{\tilde{F}_{\sqrt{t^{-1}}}}. \tag{2.51}$$

Because the total wavefield is considered as superposition of transient signals, which propagate with the same properties that the full-space Green's function, the entire wavefield must be transformed by firstly converting all the seismograms to the frequency domain by applying a Fourier transform, then multiplying them with $\tilde{F}_{\sqrt{t^{-1}}}(\omega)$ (which corresponds to a convolution in the time domain). After that, I go back to the time domain and then we apply $F_{amp_{refl}}(t)$ at time t, which means taper the seismograms with $F_{amp_{refl}}(t)$. Or we could also transform the total wavefield by first convolving all seismograms with $F_{\sqrt{t^{-1}}}(t)$ and then applying $F_{amp_{refl}}(t)$ at time t. Remember that $F_{\sqrt{t^{-1}}}(t)$ is expressed by

$$F_{\sqrt{t^{-1}}}(t) = \begin{cases} \frac{1}{\sqrt{t}} & \text{if t} \geq 0 \text{ and} \\ 0 & \text{otherwise} \end{cases}.$$

In this sense the travel path is estimated at each sample and the correct amplitude factor is applied. This is termed reflected-wave transformation. For this transformation, it is essential to know the velocity c (Forbriger et al., 2014).

b) Direct-wave transformation

The difference in the velocity of each shallow-seismic wavefield is important. For example, surface waves are generally highly dispersive and the velocity of the P-wave can differ from the phase velocity of the surface wave by up to a factor of 10. It is not appropriate to assume that we know the velocity in this case. On the other hand, it makes sense to assume a propagation path that is more or less equal to the direct wave path of a source on the surface. This approach can also be considered for reflected and refracted waves with a very small penetration depth in comparison to the source-receiver distance. The offset is therefore identical with propagation distance r. The knowledge of the travel path (offset r) and the travel-time enables us to estimate the velocity:

$$c = \frac{r}{t} \tag{2.52}$$

Substituting c in the amplitude correction expression to eliminate it, the amplitude factor hence becomes

$$F_{amp_{dir}} = \sqrt{2rc} = r\sqrt{\frac{2}{t}}. \tag{2.53}$$

$F_{amp_{dir}}$ represents the amplitude factor in the correction filter for direct waves. After remplacing this amplitude factor $F_{amp_{dir}}$ in the correction filter expressed in equation 2.42, this correction filter becomes

$$F_{Direct} = \underbrace{r\sqrt{\frac{2}{t}}}_{F_{amp_{dir}}} \underbrace{\sqrt{\frac{\pi}{\omega}}e^{i\pi/4}}_{\tilde{F}_{\sqrt{t^{-1}}}}. \tag{2.54}$$

Like the previous transformation, we first convert all the seismograms to the frequency domain, then we multiply them with $\tilde{F}_{\sqrt{t^{-1}}}(\omega)$. After that, we go back to the time domain and then we apply $F_{amp_{dir}}(t)$ at time t, that is tapering the seismograms with $F_{amp_{dir}}(t)$. This is called the direct-wave transformation.

c) Exact transformation

Knowing that the amplitude factor depends on the velocity and travel path, I will consider that both parameters are known in this case. Without any approximation of the travel path or of velocity, the amplitude factor remains the same as derived in equation 2.42.

$$F_{amp_{ex}} = \sqrt{2rc} \tag{2.55}$$

$F_{amp_{ex}}$ representes the amplitude factor for the exacte transformation. So the spreading correction filter is given by

$$F_{Exact} = \underbrace{\sqrt{2rc}}_{F_{amp_{ex}}} \underbrace{\sqrt{\frac{\pi}{\omega}} e^{i\pi/4}}_{\tilde{F}_{\sqrt{t^{-1}}}}. \tag{2.56}$$

In this case, the entire wavefield should be transformed by firstly convolving all seismograms with $F_{\sqrt{t^{-1}}}(t)$ and then applying $F_{amp_{ex}}$, that is scaling the seismograms with $\sqrt{2rc}$. This transformation should be apply for signal with single velocity.

2.6 Source time function inversion

Full-waveform inversion (FWI) is an effective tool for retrieving a high-resolution subsurface model. The accuracy of the source signal plays an important role in reaching that goal. That means we often need to estimate the source function before or during the inversion process. An inaccurate source time function estimation can hinder the convergence of FWI.

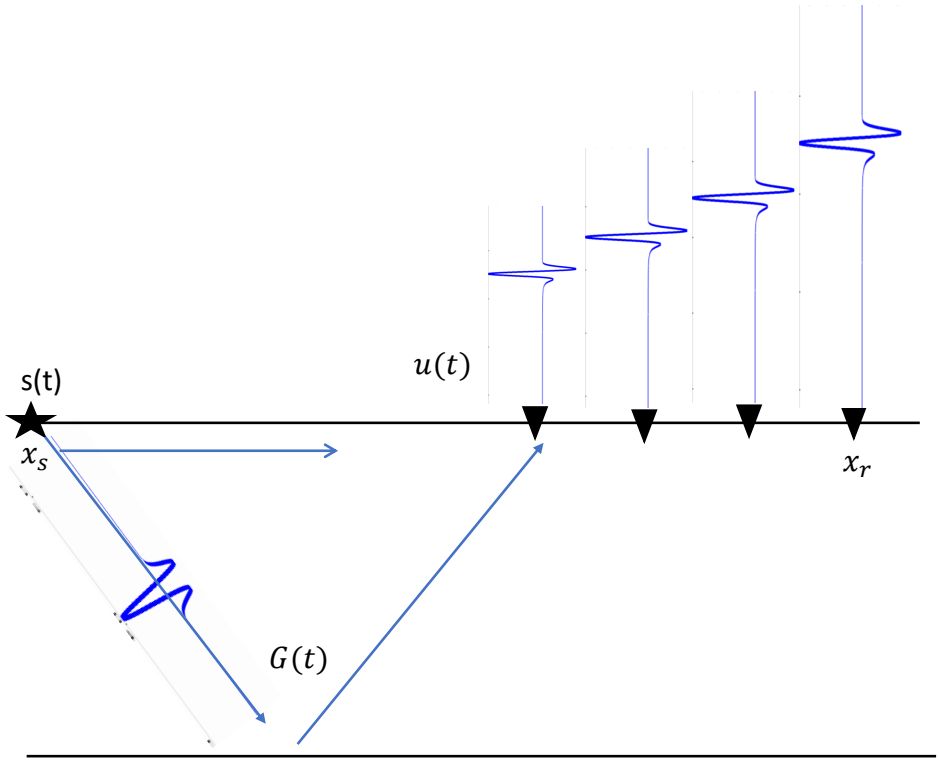

Figure 2.4: Forward modelling. $s(t)$ represents the source signal, $\vec{x_s}$ is the position of the source, $u(t)$ is the seismogram recorded at a receiver with the position $\vec{x_r}$, and $G(t)$ is the Green's function.

The combination of the Green's function with the source-time function is termed *convolution* and may be written as

$$u(\vec{x}_r, t) = s(\vec{x}_s, t) * G(\vec{x}_s, \vec{x}_r, t) \equiv \int_0^T s(\tau) G(\vec{x_s}, \vec{x_r}, t-\tau) d\tau, \tag{2.57}$$

where $u(\vec{x_r}, t)$ is the recorded seismogram, $s(\vec{x_s}, t)$ is the effective source-time function, $G(\vec{x_s}, \vec{x_r}, t)$ is the Green's function and T is the duration of the source. The source time function $s(\vec{x_s}, t)$ strongly affects the seismograms $u(\vec{x_r}, t)$. The source time-function used in field recordings is not well known in most cases and may differ for every source position (from shot to shot). This applies in particular to explosive sources and hammer blows. It can be inverted from the seismograms $u(\vec{x_r}, t)$ if the Green's function $G(\vec{x_s}, \vec{x_r}, t)$ is known. As an essential part of the FWI workflow, the source signal must be inverted simultaneously with the Green's function. The synthetic seismogram $g(\vec{x}_r, t)$ of one source at one receiver at position $\vec{x_r}$ can be calculated with the Green's function of the model m_0 via a convolution:

$$g(\vec{x_r}, t) = \int_0^T G_{m_0}(\vec{x_s}, \vec{x_r}, t-\tau) s(\tau) d\tau. \tag{2.58}$$

In the frequency domain, the convolution is expressed as a product

$$\tilde{g}(\vec{x_r}, \omega) = \tilde{G}_{m_0}(\vec{x_s}, \vec{x_r}, \omega) \tilde{s}(\omega), \tag{2.59}$$

where $\tilde{g}(\vec{x_r}, \omega)$, $\tilde{G}_{m_0}$, and $\tilde{s}(\omega)$ are the Fourier transforms of $g(x_r, t)$, $G_{m_0}(x_s, x_r, t)$, and $s(t)$, respectively. The observed seismogram $d(\vec{x_r}, t)$ can be described in the same way. The only difference is that we use the Green's function of the true model and the true source:

$$d(\vec{x_r}, t) = \int_0^T G_{m_{true}}(\vec{x_s}, \vec{x_r}, t-\tau) s_{true}(\tau) d\tau \tag{2.60}$$

In the frequency domain, we obtain:

$$\tilde{d}(\vec{x_r}, \omega) = \tilde{G}_{m_{true}}(\vec{x_s}, \vec{x_r}, \omega) \tilde{s}_{true}(\omega), \tag{2.61}$$

where $\tilde{d}(\vec{x_r}, \omega)$, $\tilde{G}_{m_{true}}(\vec{x_s}, \vec{x_r}, w)$, and $\tilde{s}_{true}(\omega)$ are the Fourier transforms of $d(\vec{x_r}, t)$, $G_{m_{true}}(\vec{x_s}, \vec{x_r}, t)$, and $s_{true}(t)$, recpectively.
The aim is to find a linear filter $C(w)$ in the frequency domain so that

$$\tilde{s}_{true}(w) - C(w)\tilde{s}(\omega) \stackrel{!}{=} \text{min}. \tag{2.62}$$

The filter $C(\omega)$ is called $source - wavelet\ correction\ filter$.
We start with the assumption that

$$\tilde{G(\omega)} := \tilde{G}_{m_0}(\omega) = \tilde{G}_{m_{true}}(\omega). \tag{2.63}$$

Then we can multiply the minimum condition with G, which gives

$$\tilde{G}(\omega)(\tilde{s}_{true}(\omega) - C(\omega)\tilde{s}(\omega)) = \tilde{d}(\omega) - C(\omega)\tilde{g}(\omega) = \text{min}. \tag{2.64}$$

The Fourier coefficients $\tilde{C}_l$ of the filter are estimated by solving a damped linear least-squares problem which is described by minimizing the objective function

$$F(\tilde{C}_l;\epsilon) = \sum_{l=0}^{N-1}\sum_{k=1}^{M} f_k^2|\tilde{d}_{lk} + \tilde{C}_l\tilde{g}_{kl}|^2 + \underbrace{M\tilde{E}\epsilon^2\sum_{l=0}^{N-1}|\tilde{C}_l|^2}_{\text{damping}} \tag{2.65}$$

with respect to the real and imaginary parts of all $\tilde{C}_l$. Thereby, $\tilde{d}_{lk}$ are the complex Fourier coefficients for the observed seismogram, $\tilde{g}_{lk}$ is the corresponding Fourier coefficient for the synthetic seismogram and N is the number of Fourier coefficient. The summation over k considers that we have multiple (M) receivers at the locations x_k. The second term is a damping term that will assure numerical stability by avoiding a division by zero. In this equation, the average energy $\tilde{E}$ of the Fourier coefficients of the synthetic seismograms is calculated by

$$\tilde{E} = \frac{1}{MN}\sum_{l=0}^{N-1}\sum_{k=1}^{M} f_k^2|\tilde{g}_{lk}|^2. \tag{2.66}$$

The function $F(\tilde{C}_l;\epsilon)$ is minimized if

$$\frac{\partial F}{\partial \tilde{C}_l} = 0. \tag{2.67}$$

This gives the coefficients of the Wiener filter

$$\tilde{C}_l = \frac{\sum_{k=1}^{M} f_k^2\tilde{g}_{kl}^*\tilde{d}_{kl}}{M\tilde{E}\epsilon^2 + \sum_{k=1}^{M} f_k^2|\tilde{g}_{kl}|^2} \tag{2.68}$$

where the synthetic and observed seismograms can be scaled with offset r_{0_k} to compensate for attenuation. The scaling coefficients f_k are defined by

$$f_k = \left(\frac{r_{0_k}}{1m}\right)^{\alpha} \tag{2.69}$$

where α is used to adjust compensation for a power law attenuation. The Fourier coefficients of an optimized source wavelet are given by $\tilde{s}^{opt} = \tilde{C}_l\tilde{s}_l$ (Groos, 2014). A stable and causal result for $\tilde{s}^{opt}$ indicates a stable convergence of the FWI workflow.

Chapter 3

Systematic study for the applicability of the 3-D/2-D transformation using the geometrical spreading correction filter derived from the Green's functions

3.1 Introduction

Seismic waves propagate in various media (homogeneous model, reflector model, or a more complex model) in different ways. To derive the geometrical spreading correction filter we assume a homogeneous acoustic medium with constant velocity. As we said in the theory part section (2.5), this filter is composed of two factors: $amplitude\ correction$ and $phase\ correction$. The amplitude factor given by $F_{amp} = \sqrt{2rc}$ depends on the travel path $r = |\vec{x} - \vec{x_s}|$ (direct distance between source and receiver), as well as on the velocity. Knowing that the wave traveling through a homogeneous model could not have the same travel path as a wave traveling through a reflector model, it would be therefore inappropriate to use the term $F_{amp} = \sqrt{2rc}$ for all types of waves. That is why for different types of waves, different approaches of the $amplitude\ correction$ have to be used. When seismic energy propagates in a reflector model, direct waves, reflected waves, transmitted waves, and other kinds of waves can be recorded. If reflected waves are recorded, their travel path r is, in the beginning, unknown and can only be calculated if we know the model velocity and the recorded time t (reflected-wave transformation). If direct waves are recorded, the velocity is not known, but the travel path r is known and equal to the offset (source-receiver distance). Consequently, the velocity can be eliminated from the amplitude factor by a substitution knowing travel path r and the recorded time (direct-wave transformation).
Before applying the spreading correction filter derived in the previous chapter to the field

data, we have to test its validity on synthetic data in order to see how well the transformation works. To illustrate the problem we will use two different models namely a homogeneous and a reflector model, which will help us to apply the different practical implementations of $amplitude\ correction$ depending on the travel path of the waves. We also need 2-D and 3-D synthetic seismograms which are calculated using two methods: The analytical solutions (solving the forward problem of acoustic wave propagation in a homogeneous model by using the Green's function) and the numerical solutions (here we solve the forward problem of acoustic wave propagation by using the finite-difference (FD) method). In this chapter, we will apply the three transformations named $exact - transformation$, $direct - wave\ transformation$, and $reflected - wave\ transformation$, developed in Chapter 2, section 2.5.1 on 3-D synthetic seismograms to test the accuracy of the transformation. Our expectation is to obtain the 2-D synthetic seismograms after we have applied the transformation.

Seismogram Comparison: analytical seismograms

In the previous chapter we derived the acoustic wave equation and through this the Green's functions in 2-D and 3-D. The knowledge of the Green's functions enables us to compute analytical solutions of the acoustic wave equation in 2-D, and 3-D using equation 2.27 at distance $x = r$ by convolution of the Green's functions with the source function.

$$P^{2D,3D}(r,0,t) = \int_{-\infty}^{+\infty} G^{2D,3D}(r,0,t) f(t-\tau) d\tau, \tag{3.1}$$

in the frequency domain that corresponds to multiplication.

$$\tilde{P}^{2D,3D}(r,0,w) = \tilde{G}^{2D,3D}(r,0,w)\tilde{f}(w), \tag{3.2}$$

where $\tilde{f}(w)$ is the Fourier transformation of the source function and $P^{2D,3D}(r,0,w)$ the analytical seismograms in the frequency domain. The green's functions were derived in the frequency domain. It will be easier to calculate first the analytical solution in the frequency domain and then apply an inverse Fourier transformation to get the analytical solution in the time domain. After computing the analytical seismograms in 2-D and 3-D, we want to convert 3-D data into 2-D data using the spreading correction filter $F(r,w)$ so that $\tilde{P}^{2D}(r,0,w) = F(r,w)\tilde{P}^{3D}$. The correction filter differs depending on cases as we demonstrated in section (2.5.1), because the travel path of each wave differs from the other.

3.2 Homogeneous model

In a homogeneous medium, the physical properties of the material do not change with the position, which means that the velocity and the density are constant. In these media, rays are

straight lines orthogonal to the wavefronts and indicate the direction of wave propagation. The path of propagation is more or less identical to the direct wave path.
For our case we assume a homogeneous acoustic medium with P-wave velocity $v_p = 1000$ m/s, and S-wave velocity $v_s = 0$ m/s because the shear modulus μ is zero in a fluid. For the acquisition, we used only one source and twenty receivers located on the right-hand side of the source with a spatial interval of 5 m. We assume that the source is located at the origin of the coordinate system with $x_s = y_s = z_s = 0$ m. The receivers with the coordinate $x_R = r$ and $y_R = z_R = 0$ are at a distance $r_0 = \sqrt{(x_R - x_S)^2 + (y_R - y_S)^2 + (z_R - z_S)^2} = |x_R - x_S|$ from the source. The model can be seen in Figure 3.1. To generate the seismogram, a shifted Ricker signal with a center frequency of $f_c = 40$ Hz was used as source wavelet. The shifted Ricker wavelet is given by the following equations:

$$\begin{aligned} f(x_x, t) &= (1 - 4\tau^2)e^{-2\tau^2}, \\ \tau &= \pi(t - t_d)f_c, \\ t_d &= 1/f_c, \end{aligned} \tag{3.3}$$

where t_d is the time delay.

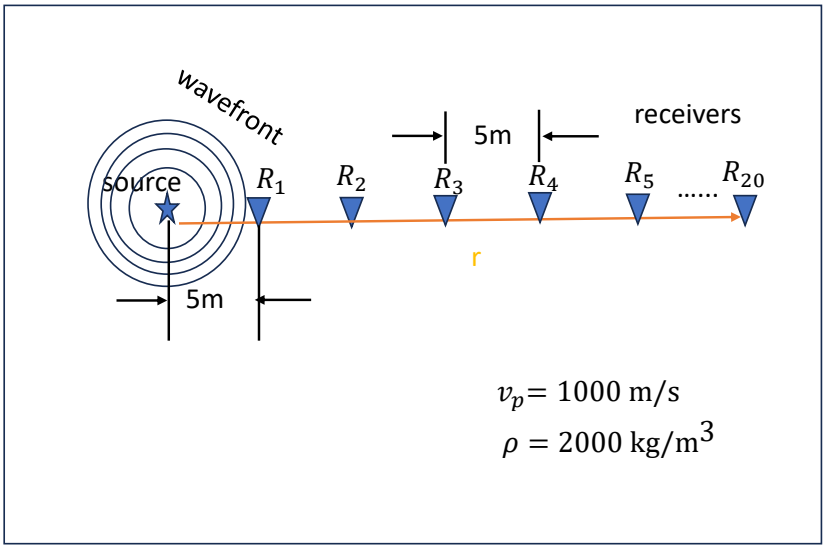

Figure 3.1: Sketch of a homogeneous full-space model. The source is marked by a star and the triangles mark the location of the receivers. The orange line represents the travel path of the direct wave

For the homogeneous model, in addition to exact transformation, I used the direct-wave transformation given respectively by the following equations in the frequency domain.

$$\tilde{P}^{2D}(r, 0, w) = F_{Exact}(r, w)\tilde{P}^{3D} = \sqrt{2rc}\sqrt{\frac{\pi}{w}}e^{-i\pi/4}\tilde{P}^{3D}(r, 0, w), \tag{3.4}$$

$$\tilde{P}^{2D}(r,0,w) = F_{Direct}(r,w)\tilde{P}^{3D} = r\sqrt{\frac{2}{t}}\sqrt{\frac{\pi}{w}}e^{-i\pi/4}\tilde{P}^{3D}(r,0,w). \tag{3.5}$$

Using the inverse Fourier transform we obtain the resulting seismograms in the time domain given by

$$P^{2D}(r,0,t) = \frac{1}{2\pi}\int_{-\infty}^{+\infty}\tilde{P}^{2D}(r,0,w)e^{iwt}\,dw. \tag{3.6}$$

3.3 Spreading correction filter applied on a shot gather

For this illustration, I used one source and twenty receivers to compute the seismograms. As mentioned earlier, I assumed a homogeneous acoustic medium with a constant velocity $v_p = 1000$ m/s. As a source function, a Ricker wavelet with a center frequency $f_c = 40$ Hz located at the origin was used. Figure 3.2 shows the source signature.

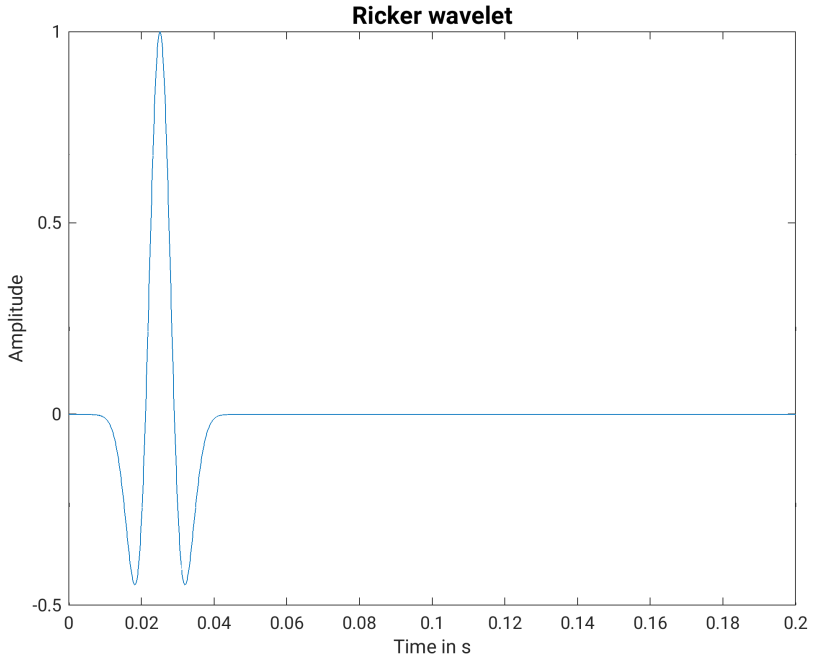

Figure 3.2: Source signal

After generating the 2-D and 3-D shotgathers composed of twenty seismograms respectively (see Figure 3.3 and Figure 3.4), I applied the exact transformation, followed by the direct-wave transformation on the 3D seismograms with the aim of obtaining seismograms that perfectly match the 2D seismograms. For a better view, we took a closer look at the seismogram with the receiver offset $r_0 = 50$ m (see Figure 3.5). The 3- D seismogram was scaled by 50 which corresponds to our distance source-receiver r_0 and the 2-D seismograms were scaled by $\sqrt{r_0}$. We can see that after scaling the 3- D seismogram by r_0, the waveform is identical to the source signature. Without this scaling an amplitude decay of r_0^{-1} will be observed. The Green's function acts like a filter, when we calculated the normalized amplitude

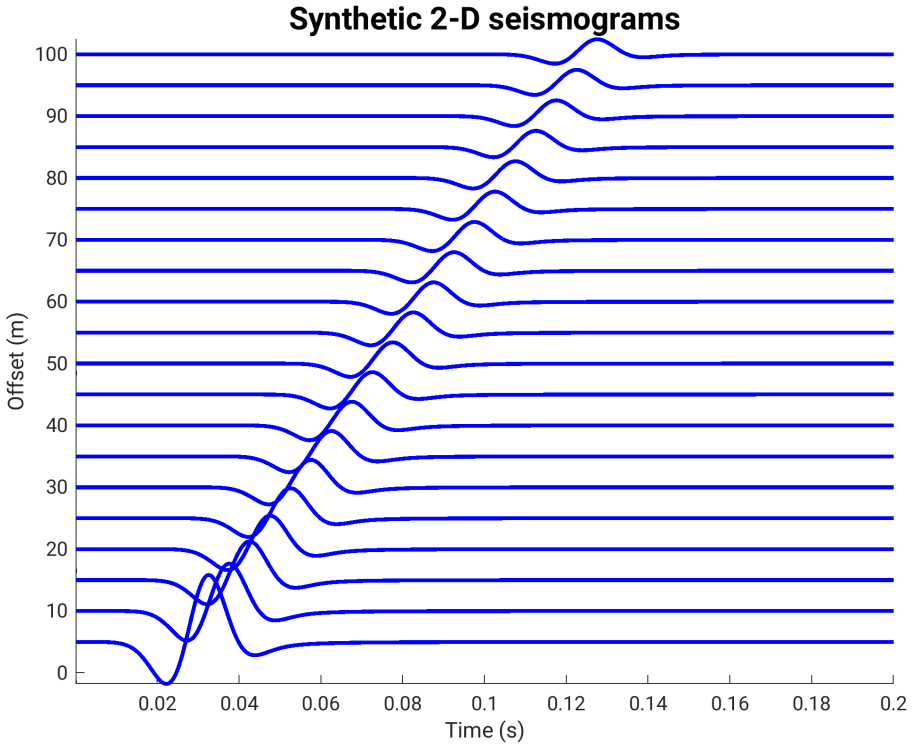

Figure 3.3: Synthetic 2-D seismograms generated by a line-source for the homogeneous model. The seismograms were computed using the analytical solution.

spectra of the 3-D Green's function, we obtained results identical to 1 ($|\tilde{G}^{3D}| \equiv 1$) this means that there is no low pass filter. Additionally looking at the equation of the 3-D green's function in the frequency domain, there is not factor that could produce a phase shift. For the 2-D analytical solution it is clearly seen that the waveform differs from the source signature, aside from that we notice an amplitude decay of $\sqrt{r_0^{-1}}$ due to the geometric spreading. Additional to that the factor $e^{\pi/4}$, which is present in the 2D Green's function in frequency domain, produces a phase shift of $\pi/4$. Finally, the normalized amplitude spectra of the 2-D Green's function is approximately $|\tilde{G}^{2D}| \approx \frac{1}{\sqrt{w}}$. Consequently, we noticed a half integration of the source wavelet which corresponds to a low-pass filter (Forbriger et al., 2014).

Figure (3.6) displays a comparison of 3-D (point-souce) seismograms (black) and 2-D (line source) seismograms (blue), Only ten traces are displayed. To emphasize the phase residuals, I normalized 3-D and 2-D seismograms to the maximum amplitude of each trace otherwise comparison would not be possible due to different decay of amplitude. Consequently, the difference in the amplitude decay with offset can not be observed. The residual seismograms between the normalized 3-D and 2-D seismograms are displayed in red. The residual seismograms are normalized too. The wavefields generated by a point source are advanced in phase with respect to the wavefield excited by a line source.

To avoid a projection of the differences in the wavefields in amplitude and phase into the reconstructed subsurface model a 3-D/2-D transformation must be applied to the recorded

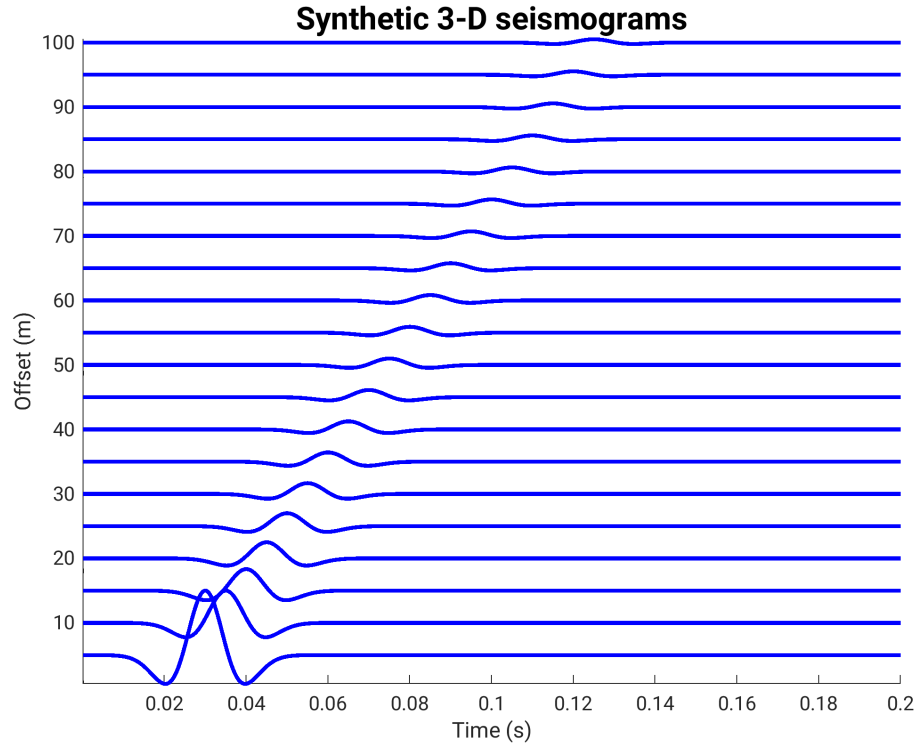

Figure 3.4: Synthetic 3-D seismograms generated by a point-source for homogeneous model. The seismograms were computed using the analytical solution.

(3-D) point-source data before applying a 2-D FWI.

The exact transformation (here we assume that the velocity and the travel path are known) was applied to 3-D seismograms and the result can be seen in Figure (3.7). For better visibility, a linear travel time correction to each time series was applied to remove the effect of the offset in the arrival times. I considered traces from three different receivers located respectively at offsets $=$ 10 m, 50 m, and 100 m (see Figure 3.8). Looking at the figure we can clearly see that after applying the exact transformation to the 3-D seismograms we achieved a result that perfectly matched the 2-D seismograms: The waveform difference has been corrected, there is no more phase shift and the amplitude from the 3-D to 2-D corrected seismograms fit perfectly with 2-D seismograms. In addition, I noticed that the correction filter worked very well regardless of the offset.

In order to quantify the relative difference between 2-D seismograms $data2D$ and the 3-D-to-2-D transformed seismograms $data3D_{corrected}$, I calculated the L2 norm error with the formula:

$$E = \frac{\sum_{l=0}^{N}(data2D - data3D_{corrected})^2}{\sum_{l=0}^{N} data2D^2}, \tag{3.7}$$

where the summation is over the offsets (distance between source and receiver). The results are shown in Figure 3.12. We can see that for the exact transformation, we have a relative

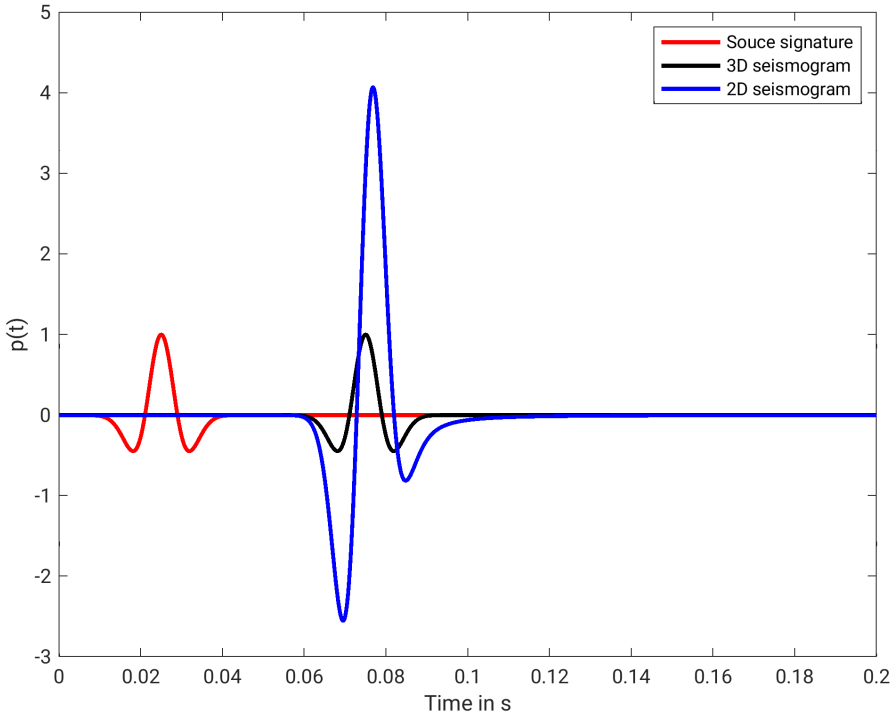

Figure 3.5: Synthetic 2-D (blue line) and 3-D (black line) seismograms were generated using the analytical solution, displayed for a single receiver which is 50 m away from a source, both sitting in a homogeneous full space. The red line represents the source signature. The 2-D wavelet is larger in amplitude and is phase shifted by $\frac{\pi}{4}$ with respect to the 3D wavelet.

percent error of 0%, which means that the 3D-to-2D corrected seismograms fit perfectly with 2-D seismograms. After testing the validity of the geometrical spreading correction filter using the exact transformation which leaves a perfect result, I also tested the validity of direct-wave transformation. Remember that for this transformation, we assumed that we did not know the velocity. But the knowledge of the travel time t and the travel path (straight path from source S to receiver R which is at a distance $r_0 = r($ travel path) from the source) enabled us to substitute the velocity c in the equation by $\frac{r}{t}$. The direct-wave transformation was also applied to 3-D seismograms and the result can be seen in Figure (3.9). For better visibility, I selected traces from three different receivers located at offsets $=$ 10 m, 50 m, and 100 m, respectively (see Figure 3.10). Looking at the figure we can see that at small receiver offset, the transformation does not work well although the phase shift and waveform have been corrected. With increasing receiver offset the transformation improves so that at $r_0 = 100$ m the corrected seismogram fits well with a 2D seismogram whether in amplitude, phase, or waveform.

There is a reason why the 3-D-to-2-D transformed seismograms and the 2-D seismograms do not fit perfectly using the direct-wave transformation. As we derived the formula of the amplitude factor for direct waves, we make an approximation. The amplitude factor in equa-

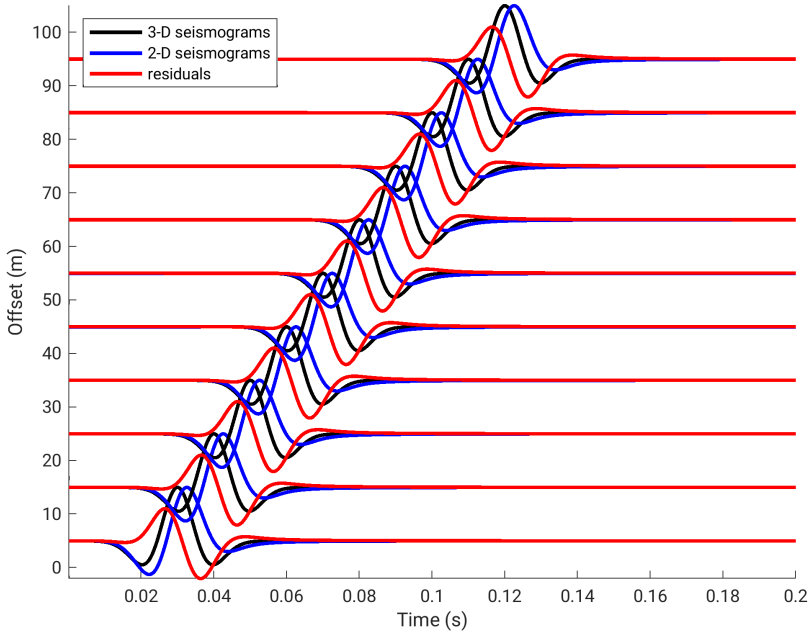

Figure 3.6: Comparison of 3-D(point-source) seismograms and 2-D (line-source) seismograms. The black seismograms are generated by a point source whereas the blue seismograms are excited by a line source. The red seismograms are the residuals between 3-D and 2-D seismograms.

tion (2.51) is based on the assumption that the arrival times of direct wave t_D time equals travel time (see Figure 3.11. This results in a time difference that leads to an error. The amplitude correction is perfect only at the time $t = t_D$. To derive the error of the direct wave correction, I take the $L2$ error.

As I mentioned in the theory part, the geometrical spreading correction filter F derived from the Green's functions in two dimensions G^2 and three dimensions G^3 should transform 3-D data into 2-D data so that $G^2 = FG^3$. This filter has two factors: Amplitude correction $F_{amp} = \sqrt{2rc}$ and the phase correction $\tilde{F}\{\sqrt{t^{-1}}\}$. We can see in Figure 3.10 that the phase shift regardless of the offset is perfectly corrected. Consequently, we made an error estimation only of the amplitude correction. The amplitude correction for the direct wave is given by:

$$F_{amp_{dir}} = \sqrt{2rc} = \sqrt{2r^2 t_D^{-1}} \equiv r\sqrt{\frac{2}{t}}. \tag{3.8}$$

Because we assumed by the correction that the arrival times of direct waves t_D equal to the travel times t, the amplitude error of the direct wave correction could be calculated as follows:

$$E_{direct} = \int_{t_D}^{t_D+T} \left(\sqrt{\frac{2}{t}} G^{3D}(t) - \sqrt{\frac{2}{t_D}} G^{3D}(t) \right)^2 dt \tag{3.9}$$

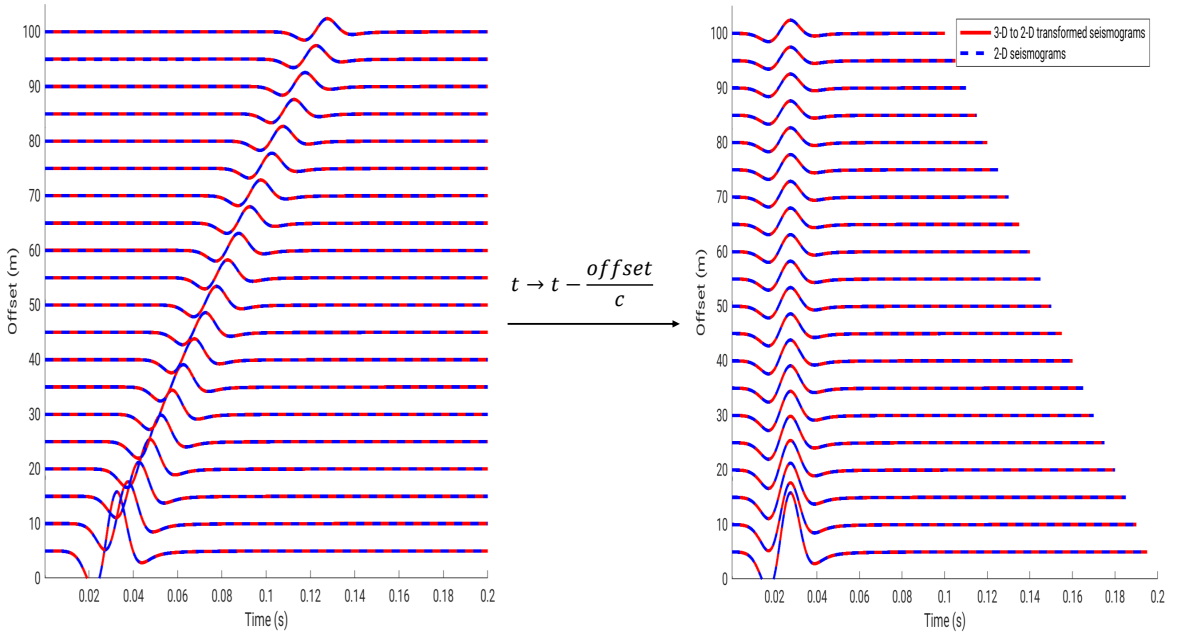

Figure 3.7: Synthetic 2-D (dashed blue line) seismograms were generated using the analytical solution and 3-D-to-2-D transformed seismograms (red line) were obtained using the exact transformation. The left plot shows seismograms at increasing source-receiver distance. the right plot shows the same profile after applying a linear traveltime correction.

$$= \int_{t_D}^{t_D+T} (G^{3D})^2(t) \left(\sqrt{\frac{2}{t}} - \sqrt{\frac{2}{t_D}} \right)^2 dt \tag{3.10}$$

Where $G^{3D}(t)$ is the Green's function for three dimensions in the time domain. To see the error of the amplitude correction only, we assume $G^{3D}(t) \equiv 1$. Equation 3.10 becomes

$$E_{direct} = \int_{t_D}^{t_D+T} \left(\sqrt{\frac{2}{t}} - \sqrt{\frac{2}{t_D}} \right)^2 dt, \tag{3.11}$$

$$= \int_{t_D}^{t_D+T} \left(\frac{2}{t} - \frac{4}{\sqrt{tt_D}} + \frac{2}{t_D} \right) dt, \tag{3.12}$$

$$= \int_{t_D}^{t_D+T} \frac{2}{t} dt - \int_{t_D}^{t_D+T} \frac{4}{\sqrt{tt_D}} dt + \int_{t_D}^{t_D+T} \frac{2}{t_D} dt, \tag{3.13}$$

$$= \left[2 \ln t \right]_{t_D}^{t_D+T} - \frac{4}{\sqrt{t_D}} \left[2\sqrt{t} \right]_{t_D}^{t_D+T} + \frac{2}{t_D} \left[t \right]_{t_D}^{t_D+T}, \tag{3.14}$$

$$= 2 \ln \left(\frac{t_D}{t_D+T} \right) - \frac{4}{\sqrt{t_D}} 2 \left[-\sqrt{t_D} + \sqrt{t_D+T} \right] + \frac{2}{t_D} \left[t_D + T - t_D \right], \tag{3.15}$$

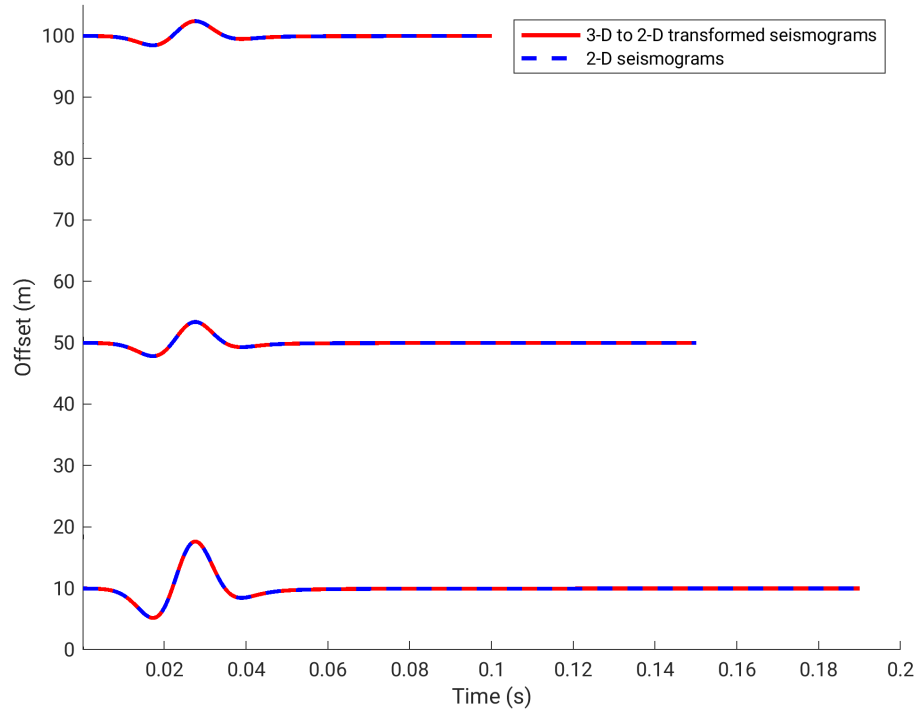

Figure 3.8: Three seismograms recorded at the source-receiver distance $r_0 = 10$ m, $r_0 = 50$ m, and $r_0 = 100$ m, respectively. Synthetic 2D (dashed blue line) seismograms were generated using the analytical solution and 3D-to-2D transformed seismograms (red line) were obtained using the exact transformation.

$$= 2\ln \underbrace{\underbrace{\frac{t_D}{t_D+T}}_{\sim 1}}_{\sim 0} + 8 \underbrace{\left(1 - \underbrace{\sqrt{\frac{t_D+T}{t_D}}}_{\sim 1}\right)}_{\sim 0} + \frac{2T}{t_D}, \tag{3.16}$$

$$E_{direct} = 2\ln\frac{t_D}{t_D+T} + 8\left(1-\sqrt{\frac{t_D+T}{t_D}}\right) + \frac{2T}{t_D} \sim \frac{2T}{t_D} \sim \frac{2T}{cr} \sim \frac{1}{r}. \tag{3.17}$$

The L2 error of direct wave correction is proportional to the inverse of the travel path r which corresponds to the offset r_0. That means with increasing offset, the error E becomes smaller. Consequently, the correction improved. We can see in Figure(3.12 the relative errors for direct-wave transformation as derived above. The error E is decreasing drastically with offsets so that at offsets above 40 m the error remains well below 5%.

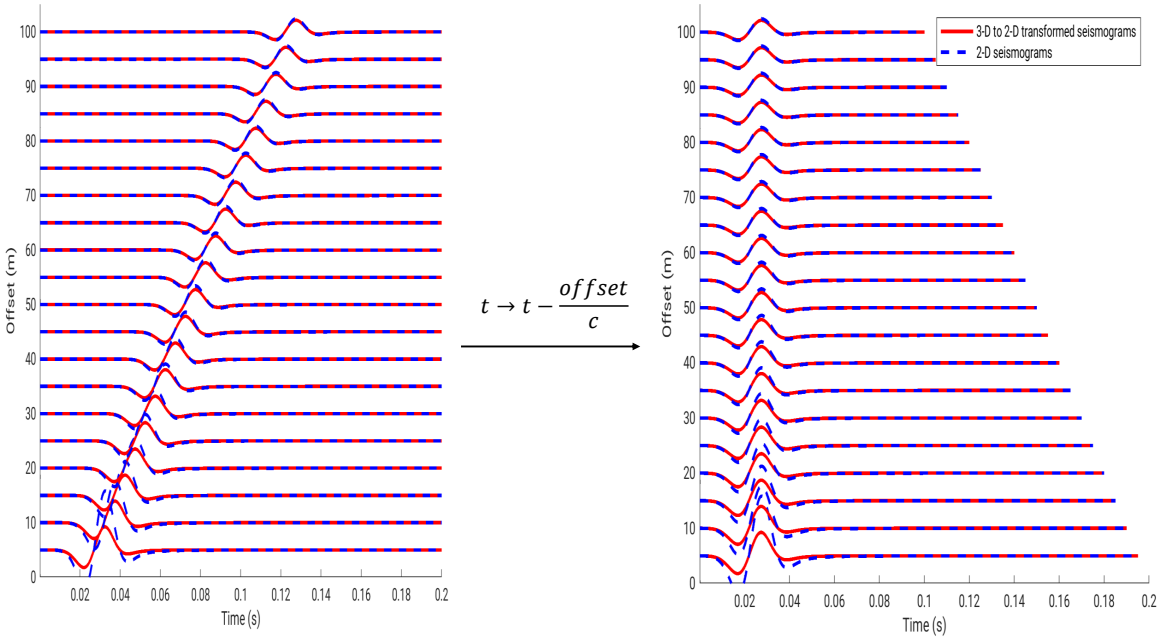

Figure 3.9: Synthetic 2D (dashed blue line) seismograms were generated using the analytical solution and 3D-to-2D transformed seismograms (red line) were obtained using the direct-wave transformation. The left plot shows seismograms at increasing source-receiver distance. the right plot shows the same profile after applying a linear traveltime correction

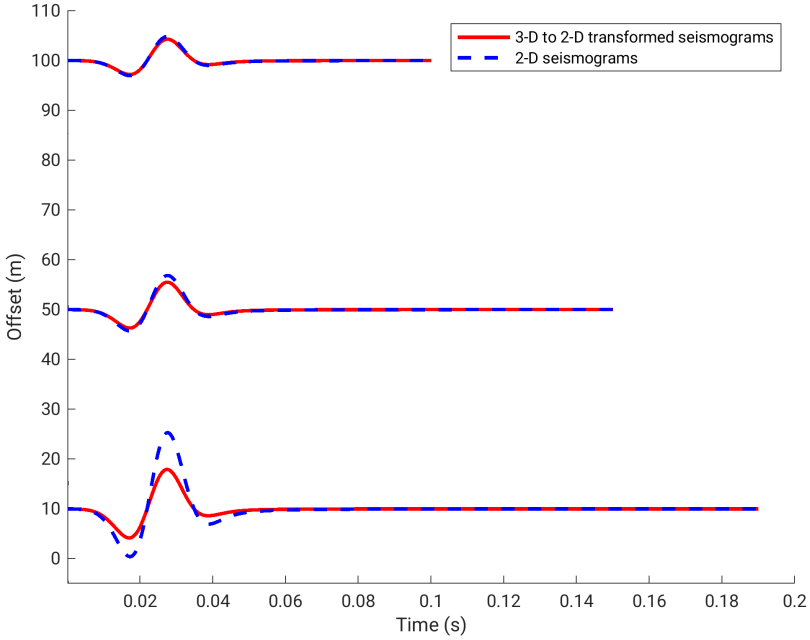

Figure 3.10: Three seismograms recorded at the source-receiver distance $r_0 = 10$ m, $r_0 = 50$ m, and $r_0 = 100$ m, respectively. Synthetic 2D (dashed blue line) seismograms were generated using the analytical solution and 3D-to-2D transformed seismograms (red line) were obtained using the direct-wave transformation.

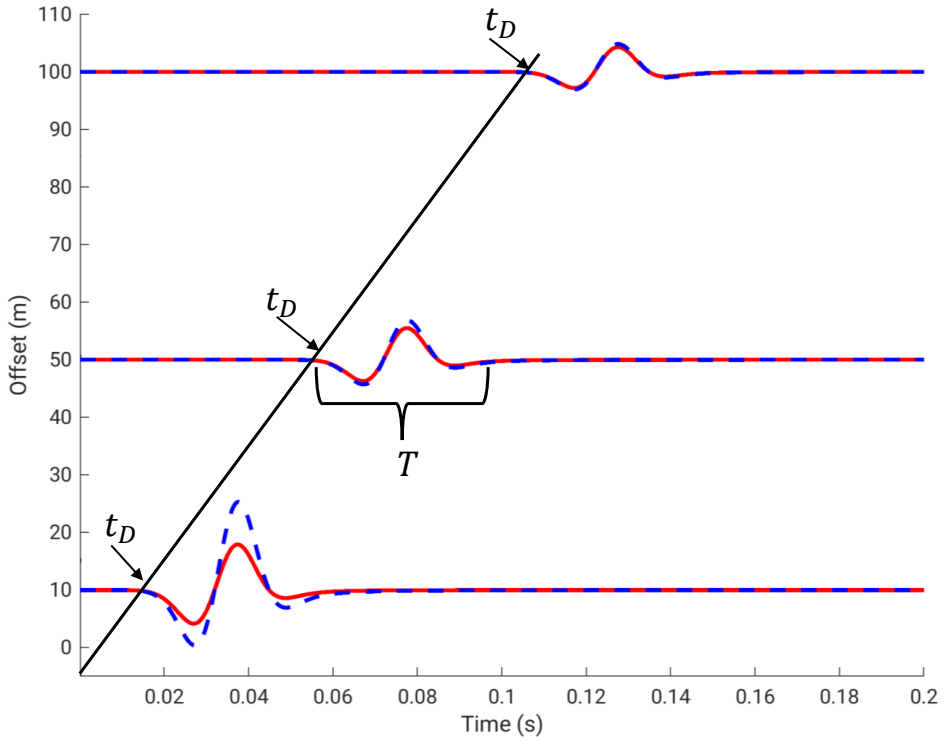

Figure 3.11: .Arrival time of the direct waves.

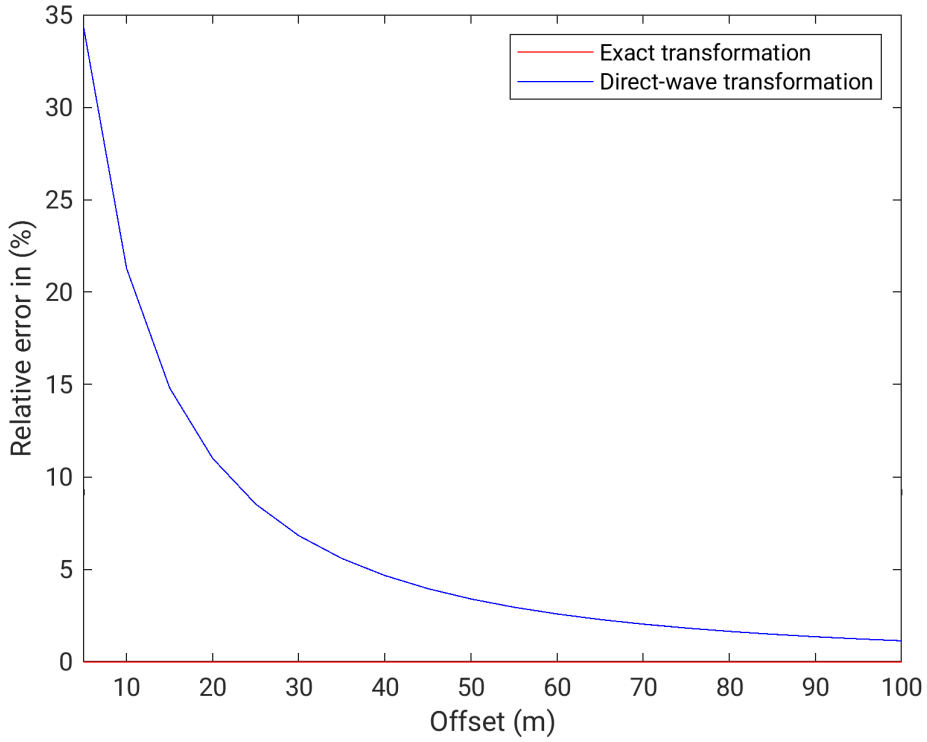

Figure 3.12: Relative errors as a function of offset for exact (red line) and direct-wave transformation (blue line) applied on point-source seismograms computed using the numerical FD method for the homogeneous Model.

Seismogram Comparison: numerical seismograms using finite-differences FD

Besides the analytical method, we also used the numerical solution to generate the seismograms. In this part, two models were used: The homogeneous and the reflector model.

3.4 homogeneous block model

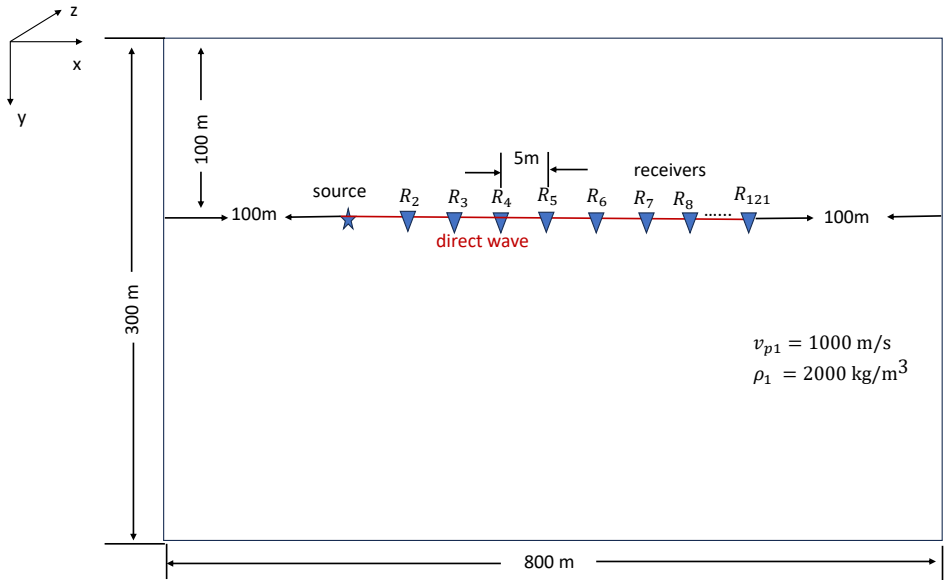

Figure 3.13: Sketch of the homogeneous block model. The source is marked by a star and the triangles mark the location of the receivers. The red line represents the travel path of the direct.

I used a simple model of a homogeneous layer. The model is 800 m in width and 300 m in depth. An explosive source is located inside the model and one hundred twenty-one receivers are located on the right-hand side of the source with an equidistant spacing of 5 m. Figure (3.13) illustrates the homogeneous block model in the case of two dimensions. To generate the synthetic seismograms for the reflector model, we used the in-house forward modeling software SOFI2D and SOFI3D, which represent, respectively, a 2D and 3D time domain massive parallel forward modeling code for P-and S-waves. It is based on a FD scheme (hence its abbreviation "Seismic modeling with FInite differences") (Bohlen et al., 2016). To calculate the wave field in the subsurface, the subsurface is divided into an equidistant grid. The Finite Difference Method approximates the derivation of the equation of motion using differential quotients at equidistant grid point. Both the partial and temporal derivatives in the wave equations are then calculated in equidistant time steps, making it numerically efficient and relatively straightforward to implement. The FD parameters I used to create the seismograms are given in Table 3.1. The homogeneous block model has the dimension 800×300 m for SOFI2D and $800 \times 200 \times 100$ m for SOFI3D. In the layer, I assumed a P-wave

Table 3.1: FD parameters.

Treatment B	Treatment A
NX: number of gridpoints in x-direction	300
NY: number of gridpoints in y-direction	800
NZ: number of gridpoints in z-direction	100
DX,DY,DZ : distance between gridpoints (in m) in x,y,z-direction	1
Spatial FD order	4
Temporal FD order	2
DT: time stepping (in s)	10^{-4}
Boundary condition	perfectly matched layer (PML)
FW: width of the absorbing frame	40
Source	Explosion(point source)
Recievers	hydrophone(pressure)

velocity of $Vp_1 = 1000$ m/s and a density $\rho_2 = 3000\ \mathrm{kg/m^3}$. Remember that we assumed that the wave propagates in fluids (acoustic case), so the S-wave velocity vanishes. For SOFI2D, the explosive source is located inside the model at point $x_S = 100$ m, $y_S = 100$ m, $z_S = 0$ m. The source function is a Ricker wavelet with a center frequency f_c of 40 Hz. The one hundred twenty-one receivers are located along a straight line, the first receiver position is defined by ($x_R = 100$ m, $y_R = 100$ m, $z_R = 0$ m), and the last receiver position by ($x_R = 700$ m, $y_R = 100$ m, $z_R = 0$ m). For SOFI3D the source and receiver locations are shifted to the middle of the block. That means that the new location of the source would be (100 m, 100 m, 50 m), and the same goes for the receivers. The synthetic 2-D and 3-D seismograms for the homogeneous model can be seen in Figures (3.14) and (3.15), respectively. Each of these seismograms is normalized to its maximum amplitude. Therefore, the difference in the amplitude decay with offset cannot be observed. Figure 3.16 displays the difference between seismograms generated by a line source (blue) and seismograms exited by a point source (black). The residual seismograms are in red. To correct the difference in amplitude, phase and wavefield between 3-D and 2-D seismograms before the application of the FWI to reconstruct the subsurface model, the 3-D/2-D transformation was applied to the 3-D (point-source) data using the direct-wave transformation. Figure 3.17 displays the results after applying the 3-D/2-D transformation using the direct-wave transformation. I applied a linear travel time correction to each time series for better visibility. The seismograms are not normalized. I considered seismograms recorded at the source-receiver distance $= 20$ m, 245 m, and 495 m (see Figure 3.18). I zoomed the traces to clearly see the difference between the transformed point-source (3-D) seismograms and the line-source (2-D) seismograms. Looking at the figure we can clearly see that after applying the direct-wave transformation to the point-source (3-D) seismograms we achieved a result that perfectly matched the line-source (2-D) seismograms in waveform and phase. The amplitude, however, does not fit very well. The difference in amplitude is due to the approximation of the amplitude correction factor for direct wave.

I also computed the L2 norm with the formula:

$$E = \frac{\sum_{l=0}^{N}(data2D - data3D_{corrected})^2}{\sum_{l=0}^{N} data2D^2}, \tag{3.18}$$

, to quantify the difference between 2-D seismograms $data2D$ and the 3-D-to-2-D transformed seismograms $data3D_{corrected}$. The result can be seen in Figure 4.6. Look at the figure we can see that the error E is decreasing with offsets so that at offsets above 100 m the error remains well below 10%

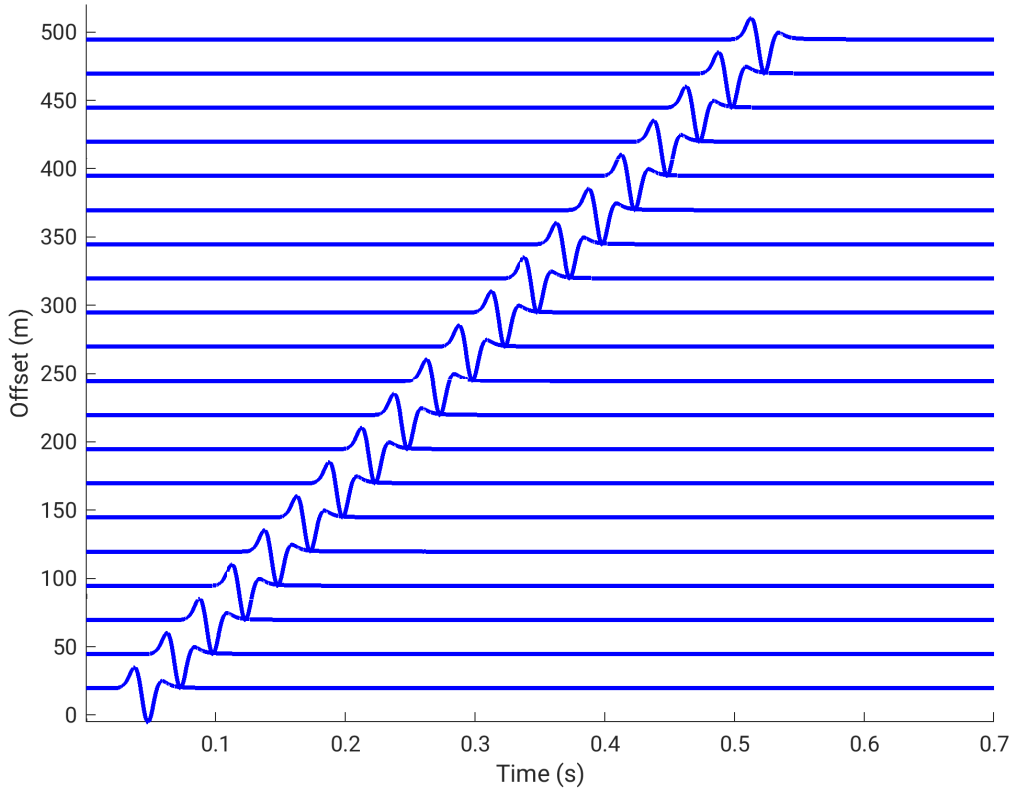

Figure 3.14: Synthetic 2-D (line source) seismograms generated using the numerical FD method for the homogeneous block model. The seismograms were normalized to the maximum amplitude of each trace.

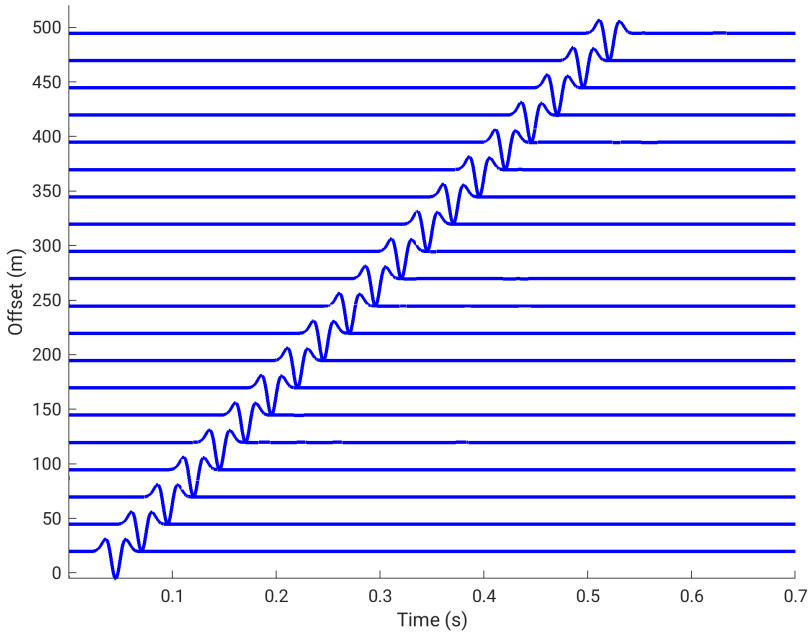

Figure 3.15: Synthetic 3-D (point source) seismograms generated using the numerical FD method for the homogeneous block model.The seismograms were normalized to the maximum amplitude of each trace.

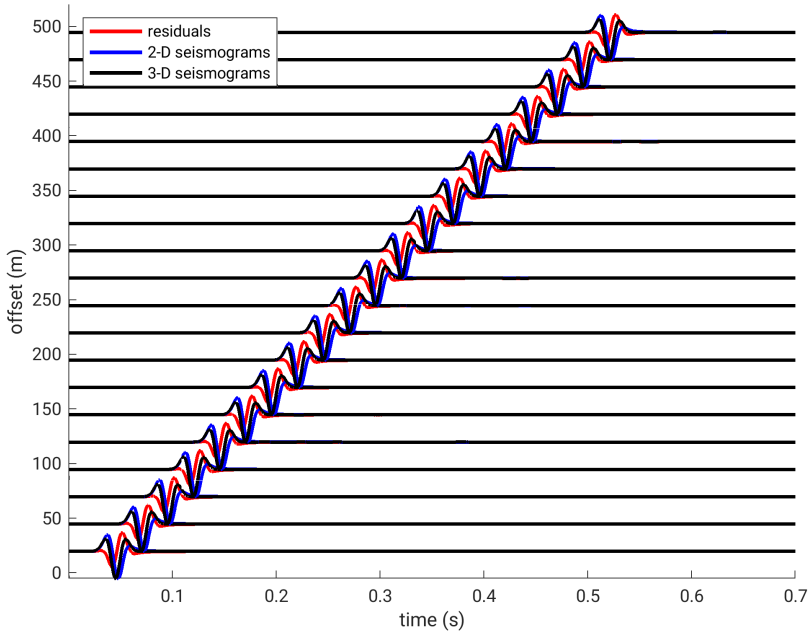

Figure 3.16: Comparison of 3-D(point-source) seismograms and 2-D (line-source) seismograms. The black seismograms are generated by a point source whereas the blue seismograms are excited by a line source. The red seismograms are the residuals between 3-D and 2-D seismograms.

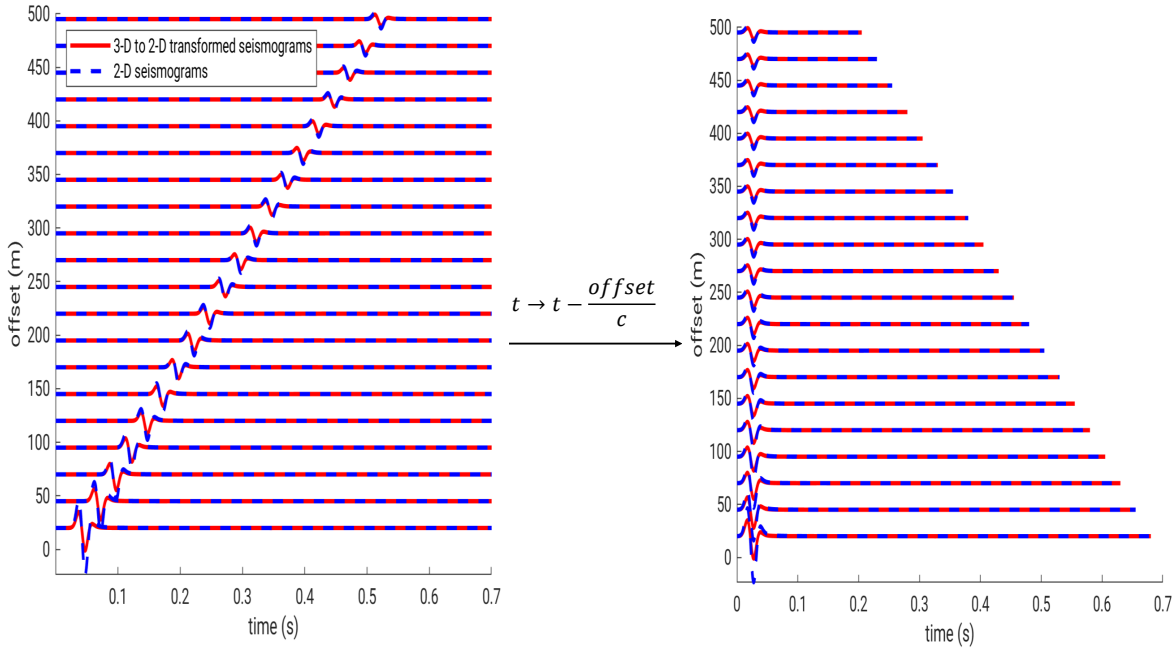

Figure 3.17: Synthetic 2D (dashed blue line) seismograms were generated using the numerical the FD method and 3D-to-2D transformed seismograms (red line) were obtained using the direct-wave transformation. The left plot shows seismograms at increasing source-receiver distance. the right plot shows the same profile after applying a linear travel time correction.

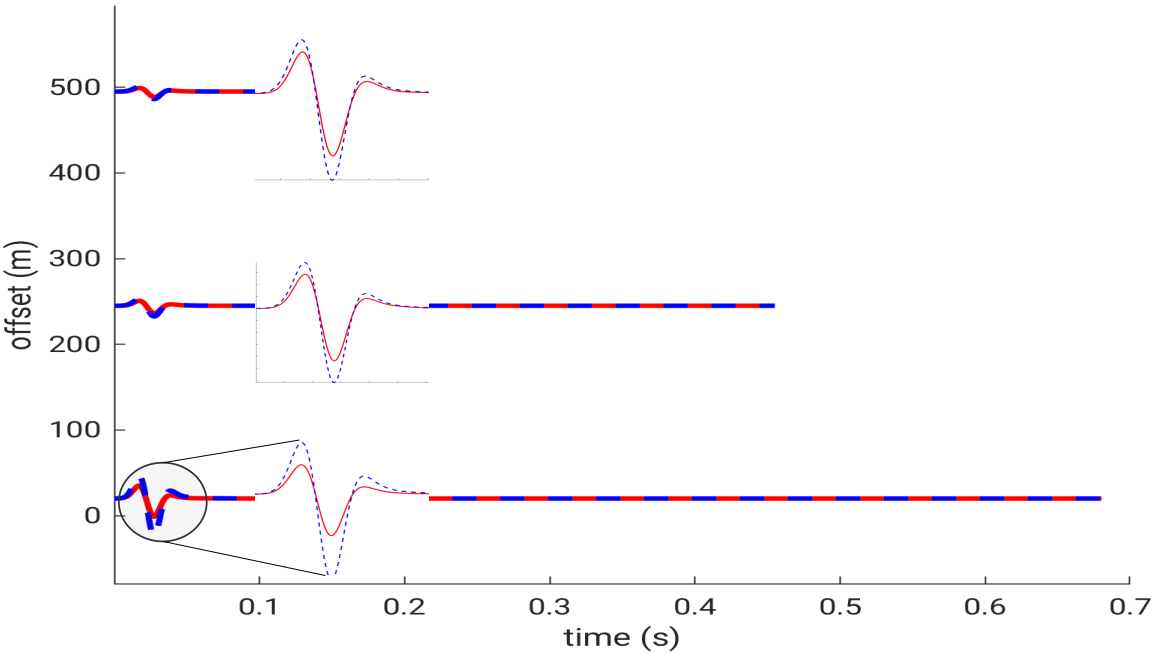

Figure 3.18: Three seismograms recorded at the source-receiver distance $r_0 = 20$ m, $r_0 = 245$ m, and $r_0 = 495$ m, respectively. Synthetic 2D (dashed blue line) seismograms were generated using the numerical FD method and 3D-to-2D transformed seismograms (red line) were obtained using the direct-wave transformation.

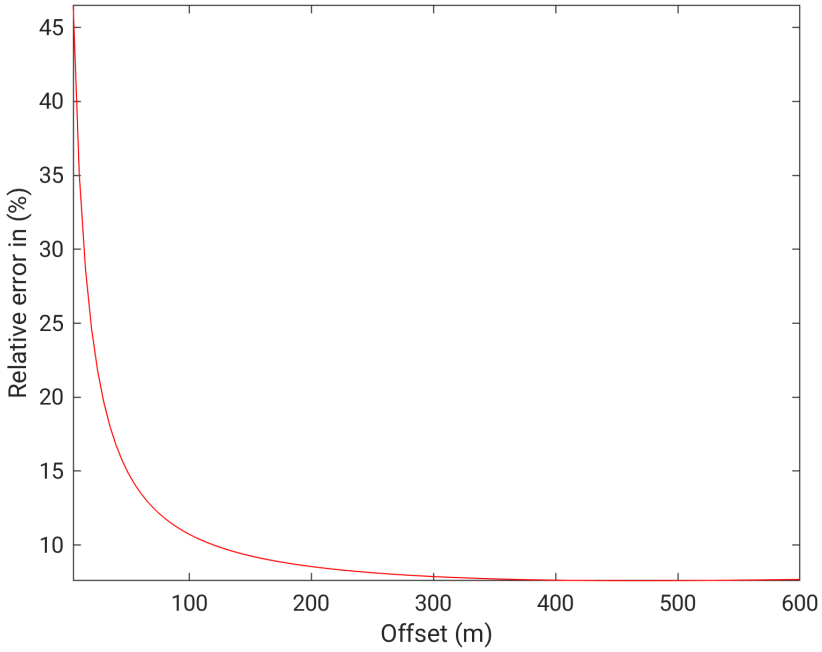

Figure 3.19: Relative errors as a function of offset for direct-wave transformation applied on point-source seismograms computed using the numerical FD method for the homogeneous Model.

3.5 Reflector block model

Besides the homogeneous model, I also used a reflector model. The model is 800 m in width and 300 m in depth with two layers. The first layer is 200 m thick and the second layer is 100 m thick. An explosive source is located inside the model and one hundred twenty-one receivers are located on the right-hand side of the source with a spatial interval of 5 m. In Figure (3.20) we can see the illustration of the two-layered model in the case of two dimensions. When seismic energy travels through different media at different velocities, part of the energy is refracted and transmitted through the interface, and part of the energy is reflected back towards the surface at the interfaces where the media velocity and/or density changes. The amplitude and polarity of the reflection depend on the change of the impedance, which is the product of the velocity and the density, across an interface. At a particular angle of incidence called the critical angle there is no transmission and all the energy is either reflected or travels along the boundary between the layers as a head wave. I used the same FD

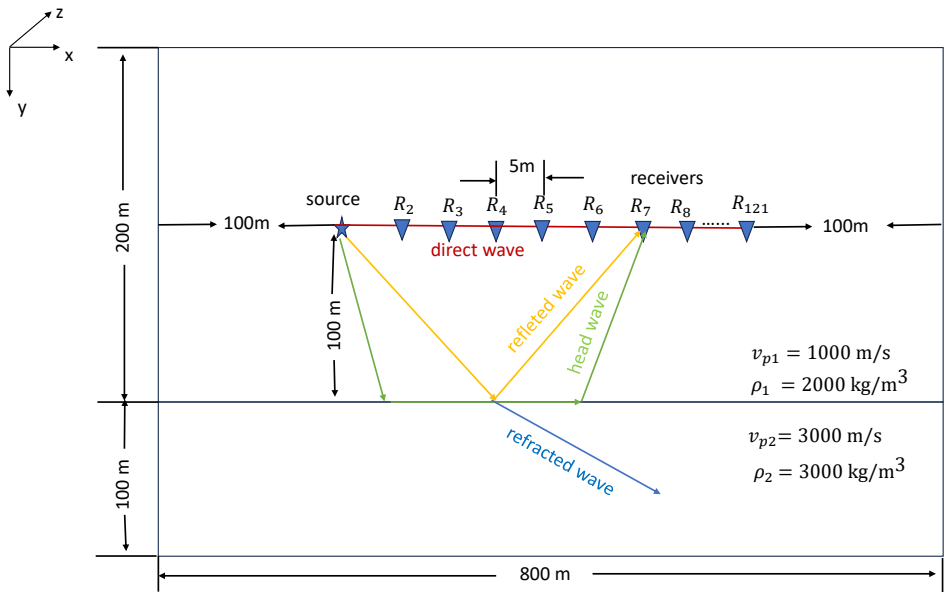

Figure 3.20: Sketch of the reflector model. The source is marked by a star and the triangles mark the location of the receivers. The red, blue, orange, and green lines represent, respectively, the travel path of the direct, transmitted, reflected, and head waves.

parameters as for the homogeneous model to compute the 2-D and 3-D seismograms. The reflector block model has the dimension 800×300 m for SOFI2D and $800 \times 200 \times 100$ m for SOFI3D. The material parameters that I used are P-wave velocity $Vp_1 = 1000$m/s and density $\rho_1 = 2000\,\mathrm{kg/m^3}$ for the first layer and P-wave velocity $Vp_2 = 3000$ m/s and density $\rho_2 = 3000\,\mathrm{kg/m^3}$ for the second layer. As for the homogeneous model, the explosive source is located inside the model at point $x_S = 100$ m, $y_S = 100$ m, $z_S = 0$ m. The source function is a Ricker wavelet with a center frequency f_c of 40 Hz. The wavefields are recorded by one hundred twenty-one receivers located along a straight line with an equidistant spacing of 5m. The smallest source-receiver distance is 0 m and the largest is 600 m. In Figure 3.21 we can

see how the wave propagates at different times in the reflector model. At the top, we can see the spherical wavefront because a source point was used. When the wave meets the interface we see that part of the energy is reflected and goes back towards the surface (reflected wave) and part is transmitted through the interface, a little further on we notice also the presence of head wave, which travels along the boundary between the layers.

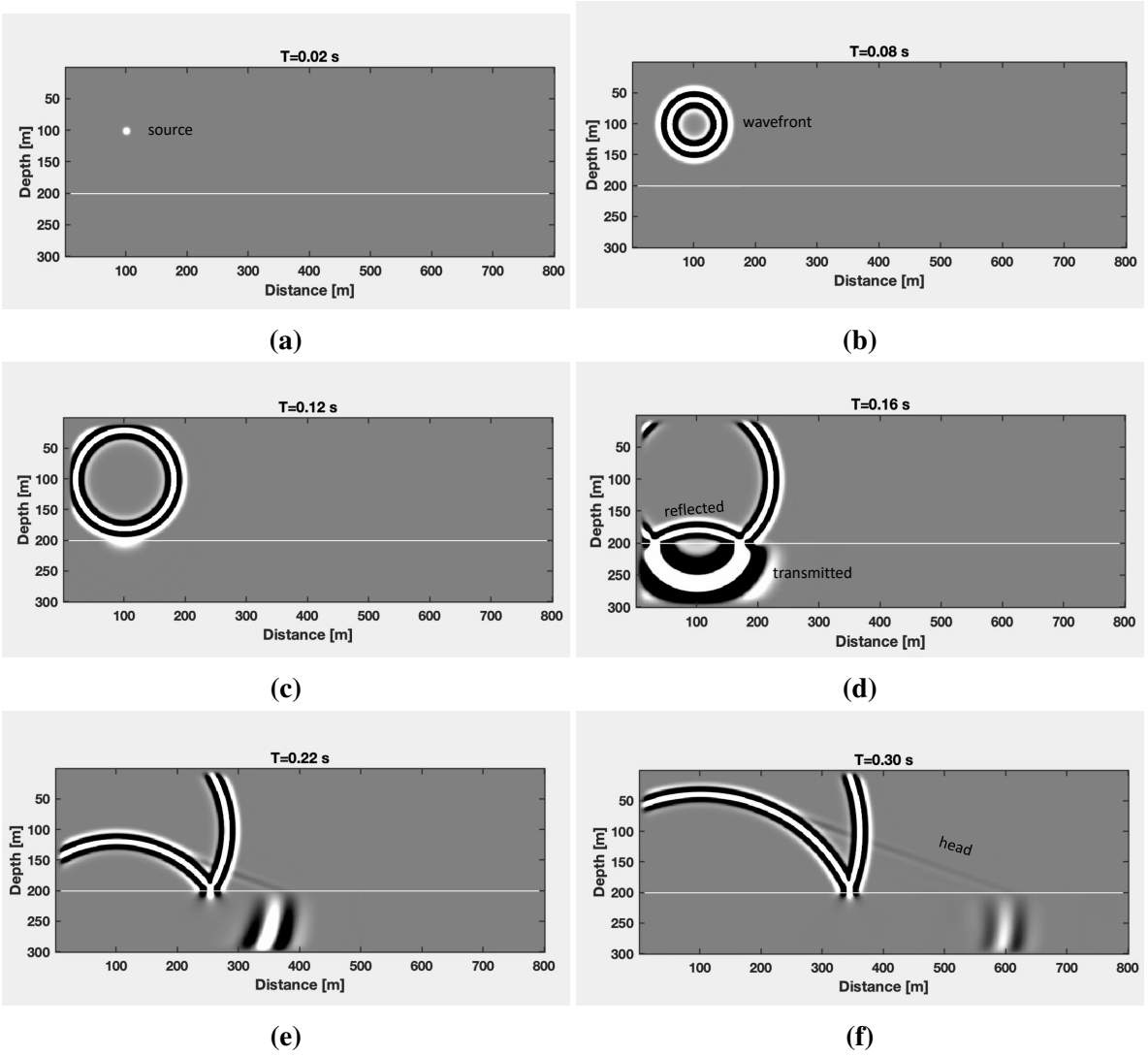

Figure 3.21: Snapshot of the 2-D wavefield for the reflector model at different times.

The 2-D and 3-D synthetic generated seismograms using the forward modeling software SOFI2D and SOFI3D can be seen in Figure 3.22 and 3.23, respectively. Because of the presence of a reflecting interface, we no longer have just direct waves, we also have reflected, transmitted, and head waves (it is difficult to identify them on the seismograms). In this part, we only need to work with the reflected waves in order to test the validity of the reflected-wave transformation. To obtain only seismograms with reflected waves, I made a subtraction between synthetic seismograms for the reflector model and the homogeneous model. The result can be seen in Figures(3.25 and (3.24) for 2-D and 3-D, respectively. Af-

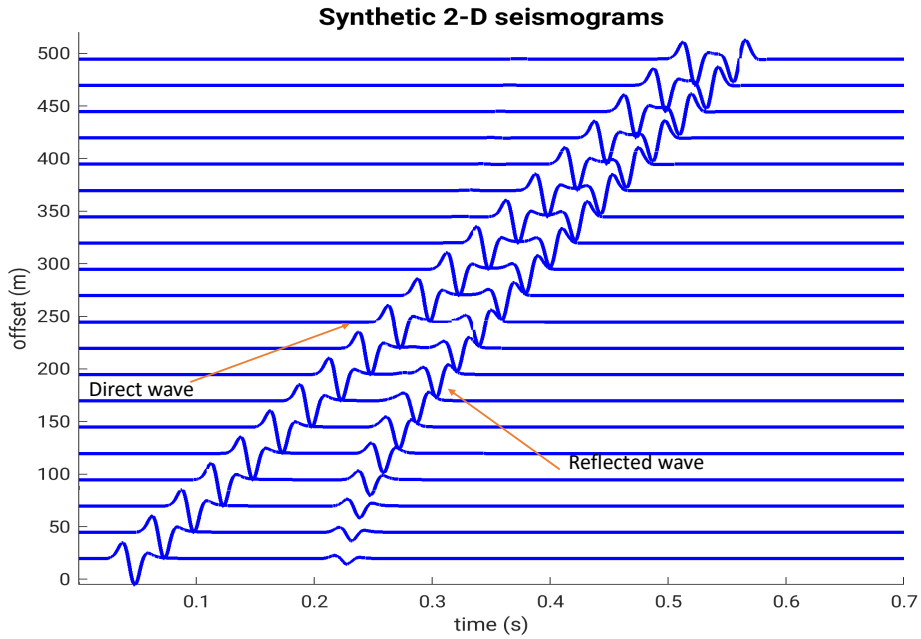

Figure 3.22: Synthetic 2-D seismograms generated using the numerical FD method for the reflector model.

ter extracting only the reflected waves, I applied the geometrical spreading correction filter using the reflected-wave transformation. Remember that for this transformation we do not know the travel path, but the knowledge of the travel time t and the velocity c enabled us to substitute the travel path $r = ct$ in the amplitude factor $F_{amp} = \sqrt{2rc}$ of the correction filter so that the amplitude correction for reflected waves $F_{ampr_{refl}}$ becomes

$$F_{amp_{refl}} = \sqrt{2rc} = c\sqrt{2t}. \tag{3.19}$$

With the purpose of obtaining the 2-D seismograms, I applied the reflected-wave transformation on the 3D seismograms with only reflected waves using the following eqaution:

$$\tilde{P}^{2D}(r,0,\omega) = F_{Reflected}(r,\omega)\tilde{P}^{3D} = c\sqrt{2t}\sqrt{\frac{\pi}{\omega}}e^{-i\pi/4}\tilde{P}^{3D}(r,0,w). \tag{3.20}$$

Using the inverse Fourier transform I obtained the resulting seismograms in the time domain given by

$$P^{2D}(r,0,t) = \frac{1}{2\pi}\int_{-\infty}^{+\infty}\tilde{P}^{2D}(r,0,w)e^{iwt}\,dw.$$

The result can be seen in Figure(3.26). To make the result more visible, I applied a hyperbolic travel time correction given by:

$$t_{nmo} = t_0\sqrt{1+\left(\frac{r_0}{ct_0}\right)^2} - t_0. \tag{3.21}$$

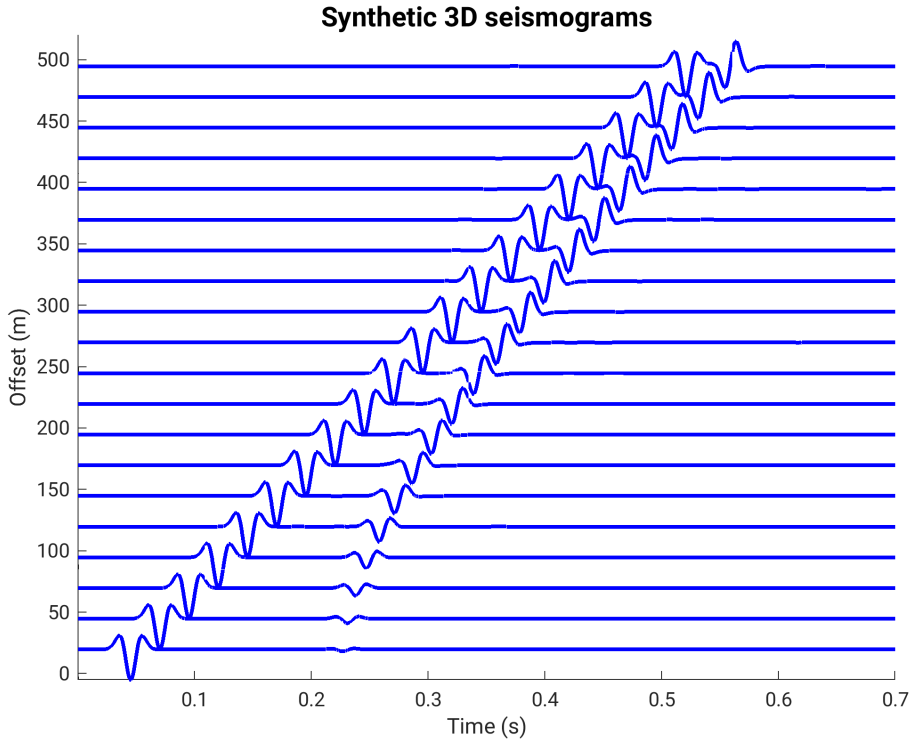

Figure 3.23: Synthetic 3-D seismograms generated using the numerical FD method for the reflector model.

With $t_0 = \frac{2d}{c}$, which is the minimum travel time, defined by the two-way vertical ray path. the parameters d, r_0, and c represent the thickness of the layer, the source-receiver distance, and the velocity, respectively. I considered three traces recorded at source-receiver distances 5 m, 250 m, and 500 m, respectively (see Figure 3.27. The figure shows us that the reflected-wave transformation works pretty well. Visually we can say that the waveform, the phase shift, and the amplitude are perfectly corrected regardless of the offset. To also quantify the result, I estimated the reflected wave error using the L2norm. For the derivation of the reflected-wave transformation, we made an approximation too. We assumed that the arrival time of the reflected waves t_R was equal to the travel time t. That means we used the arrival time of the reflected wave to correct the whole signal which introduced an error in the correction (see Figure 3.27). To derive the amplitude correction for the reflected wave we substituted the travel path r by $r = ct$ because we do not know the travel path but we know the velocity and the travel time. this amplitude correction is given by:

$$F_{amp_{refl}} = \sqrt{2rc} = \sqrt{2c^2 t_R} = c\sqrt{2t_r} \equiv c\sqrt{2t}. \tag{3.22}$$

Because The amplitude correction is based on the assumption that the arrival time t_R equals travel time t, the amplitude error of the reflected wave correction could be calculated as follows:

$$E_{refleted} = \int_{t_R}^{t_R+T} \left(c\sqrt{2t} G^{3D}(t) - c\sqrt{2t_R} G^{3D}(t) \right)^2 dt \tag{3.23}$$

$$= \int_{t_R}^{t_R+T} (G^{3D})^2(t) \left(c\sqrt{2t} - c\sqrt{2t_R} \right)^2 dt \tag{3.24}$$

Where $G^{3D}(t)$ is the Green's function for three dimensions in the time domain. We assumed $G^{3D}(t) \equiv 1$ because we only wanted to see the error of the amplitude correction. Equation 3.24 becomes

$$E_{reflected} = \int_{t_R}^{t_R+T} \left(\sqrt{2t} - \sqrt{2t_R} \right)^2 dt = \int_{t_R}^{t_R+T} \sqrt{2} \left(\sqrt{t} - \sqrt{t_R} \right)^2 dt, \tag{3.25}$$

$$= \int_{t_R}^{t_R+T} \left(t - 2\sqrt{tt_R} - t_R \right) dt = \int_{t_R}^{t_R+T} t dt - 2 \int_{t_R}^{t_R+T} \sqrt{tt_R} dt + \int_{t_R}^{t_R+T} t_R dt, \tag{3.26}$$

$$= \sqrt{2} \left[\frac{1}{2} t^2 \right]_{t_R}^{t_R+T} - 2\sqrt{t_R} \left[\frac{2}{3} t^{2/3} \right]_{t_R}^{t_R+T} + t_R \left[t \right]_{t_R}^{t_R+T}, \tag{3.27}$$

$$= \sqrt{2} \left[\underbrace{\frac{1}{2} t_R T}_{\sim t_R} + \frac{1}{2} T^2 - \frac{4}{3} \sqrt{t_R} \underbrace{\left((t_R + T)^{3/2} - t_R^{3/2} \right)}_{\sim \sqrt{t_R}} + t_R T \right] \tag{3.28}$$

$$E_r e f l e c t e d = \sim t_R \sim \sqrt{r_0} \tag{3.29}$$

because t_R is the travel time of reflected wave and is given by :

$$t_R^2 = \frac{r_0^2}{c^2} + t_0^2 \tag{3.30}$$

$$t_R = \sqrt{\frac{r_0^2}{c^2} + t_0^2} \sim \sqrt{r_0}. \tag{3.31}$$

The amplitude error of the reflected wave correction can be seen in figure(3.28). I expected a curve that continuously increases with the source-receiver distance but we noticed that the curve first began to decrease until the offset $r_0 = 100$ m and then increased continuously with the source-receiver distance. However, its value remains below 2%.

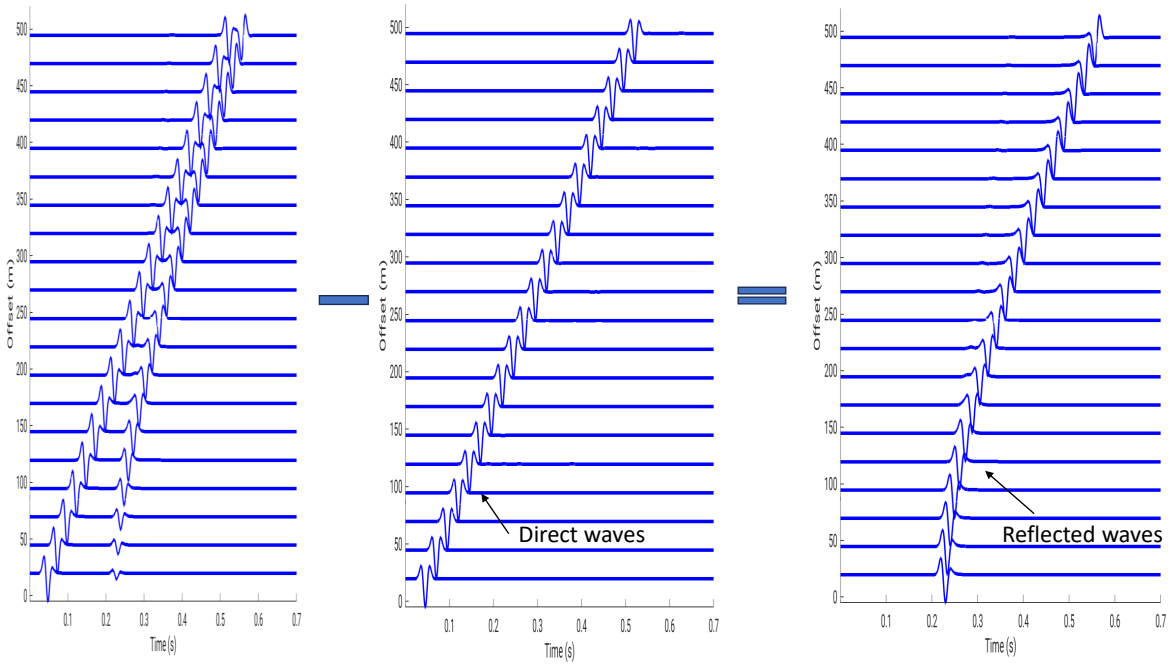

Figure 3.24: Subtraction between synthetic 3-D seismograms for the reflector model and homogeneous model to obtain seismograms only with reflected waves.

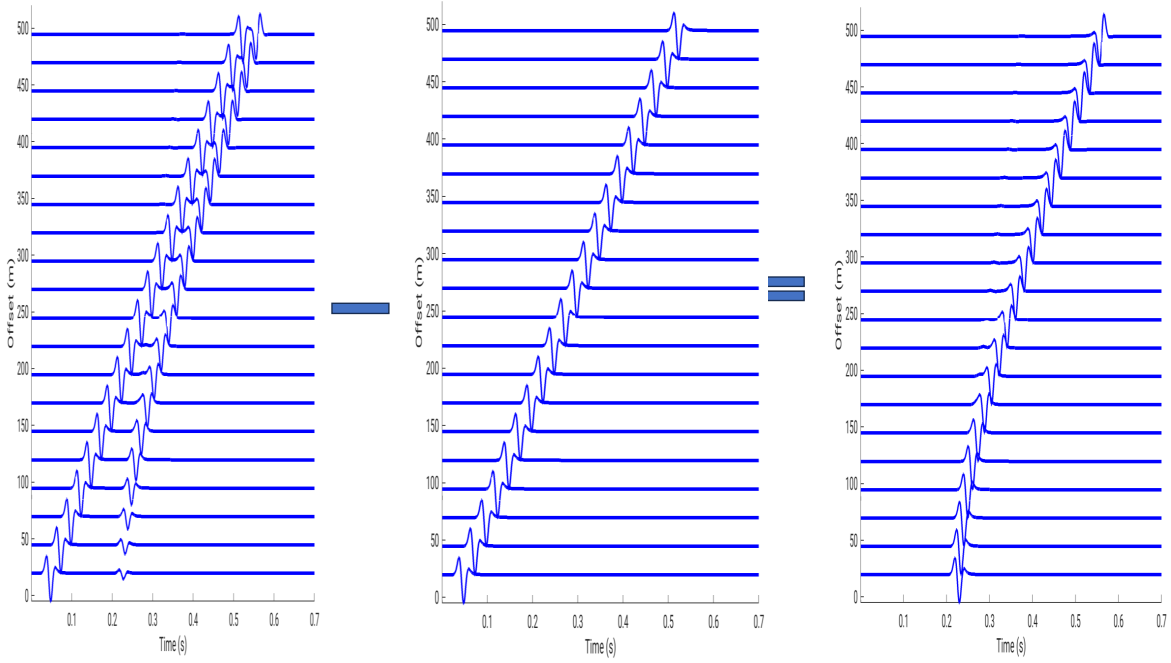

Figure 3.25: Subtraction between synthetic 2-D seismograms for the reflector model and homogeneous model to obtain seismograms only with reflected waves.

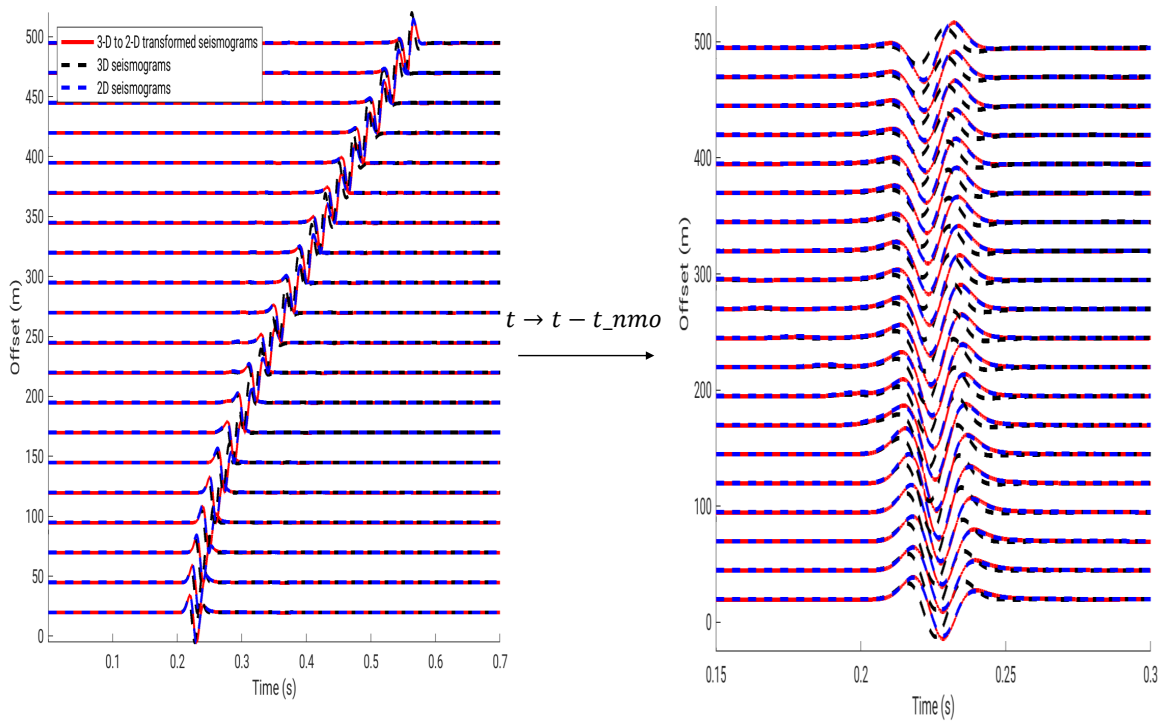

Figure 3.26: .Synthetic 2D (dashed blue line) and Synthetic 3D (dashed black line) seismograms were generated using the analytical solution. 3D-to-2D transformed seismograms (red line) were obtained using the reflected-wave transformation. The left plot shows seismograms at increasing source-receiver distance. the right plot shows the same profile after applying a hyperbolic traveltime correction

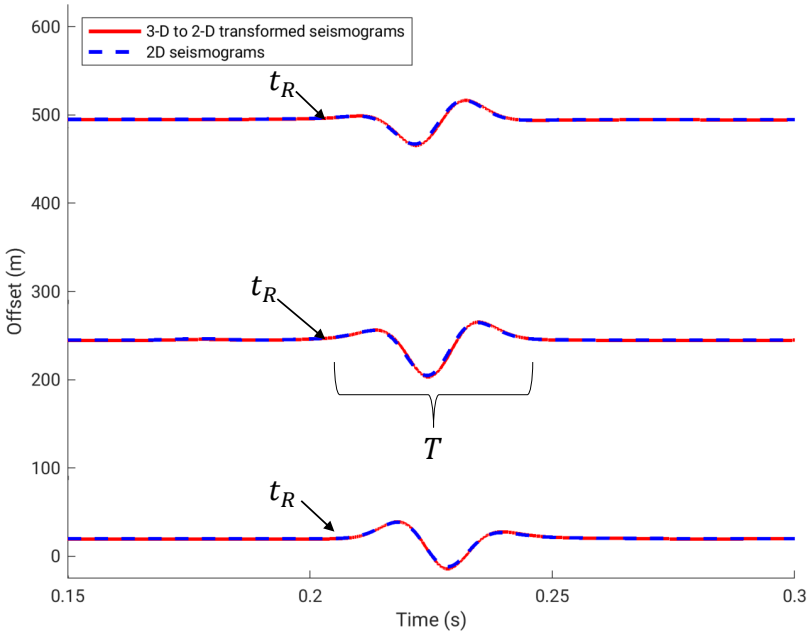

Figure 3.27: Three seismograms recorded at the source-receiver distance $r_0 = 5$ m, $r_0 = 250$ m, and $r_0 = 500$ m, respectively. Synthetic 2-D (dashed blue line) seismograms were generated using the analytical solution and 3D-to-2D transformed seismograms (red line) were obtained using the reflected-wave transformation.

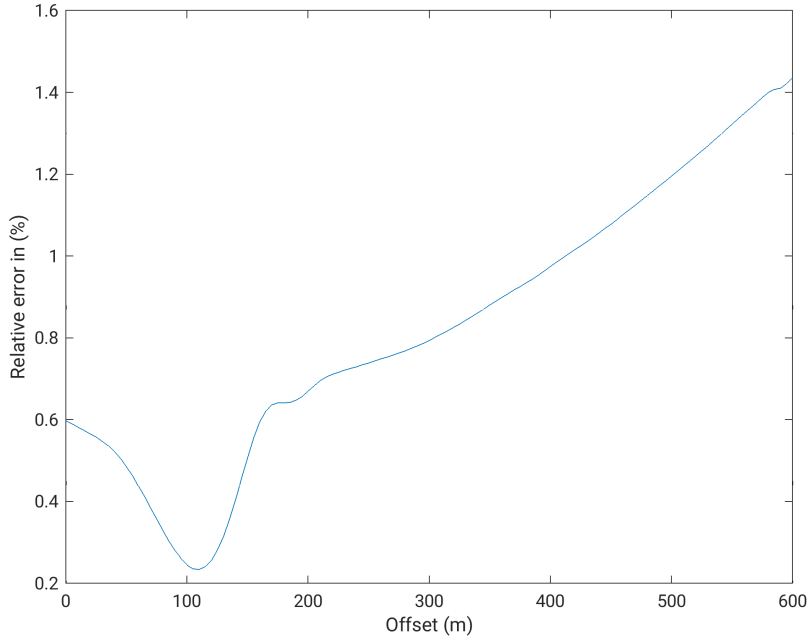

Figure 3.28: Relative errors as a function of offset for the reflected-wave transformation applied on point-source seismograms computed using the numerical FD method for the reflector Model .

3.6 Summary and discussion

In this chapter, I evaluated the accuracy of the 3-D/2-D transformation using a geometry spreading correction filter derived from 2-D and 3-D Green's functions in the frequency domain. In this method, Each point source seismogram is convolved with $\sqrt{t^{-1}}$ where t is the travel time. This action corresponds to a phase shift of $\frac{\pi}{4}$ with the purpose of correcting the phase differences between the point source seismogram and line source seismogram. The amplitude correction factor F_{amp} is afterward applied to adjust the amplitudes. The amplitude factor F_{amp} can be interpreted and applied differently. If we assume that the velocity c of the model is known, the amplitude factor in this case is $F_{amp} = \sqrt{2rc}$ where r is the offset (distance between the source and the receiver). In this work, I call this transformation $exact\ transformation$ but (Forbriger et al., 2014) call it $single - velocity\ transformation$. Since shallow-seismic wavefield often cover a range of different phase velocities, it is not appropriate to assume that we know the velocity. This transformation is not suited for all types of waves. For direct waves, the wave propagation distance equals the source-receiver distance r and therefore known. We can thus eliminate the unknown velocity c in the amplitude correction factor via $c = \frac{r}{t}$ where t is the travel time. This yields $F_{amp_{dir}} = r\sqrt{\frac{2}{t}}$. This technique is called $direct - wave\ transformation$ (Forbriger et al., 2014). For reflected waves, their travel path r is in the beginning unknown and can only be calculated if we know the model velocity. With an average velocity c and the recorded time t, the travel path is $r = ct$. We substitute r in the amplitude correction term to eliminate it, so that the amplitude factor becomes $F_{amp_{refl}} = 2\sqrt{2t}$. This transformation is called $reflected - wave\ transformation$ (Forbriger et al., 2014).

Exact transformation

This transformation was used on 3-D synthetic seismograms calculated using the analytical solution for a homogeneous model. The result is that the exact transformation works perfectly well for a homogeneous model. The waveform, the amplitude, and the phase differences between 3-D (point source) and 2-D (line source) seismograms are corrected. With a relative percent error of 0% we can conclude that the transformed 3-D seismograms into 2-D seismograms match the 2-D synthetic seismograms perfectly.

Direct-wave transformation

For this transformation, the 3-D seismograms that I used were computed using the analytical solution and the numerical FD method for a homogeneous model. For analytical seismograms, I noticed a perfect correction for the waveform and the phase shift, but I observed a slight difference im amplitude between the transformed point-source seismograms and the line-source seismograms. The accuracy of amplitude correction depends on the off-

set because the correction improves with increasing source-receiver distance. At a certain source-receiver distance the relative percent error remain below 2% that means the 3-D-to-2-D (transformed) seismograms and the 2-D seismograms match very well. For numerical seismograms, we notice that the differences in waveform and phase between 3-D and 2-D seismograms are also corrected, but the residuals in amplitude are not completly corrected. The relative percent error decreases with increasing offset so that at offset above 100 m it remains under 10%. In conclusion, the $direct - wave\ transformation$ works well.

Reflected-wave transformation

This transformation was used only for the reflector model on reflected waves. The seismograms were computed using the numerical FD method. This transformation was applied on (point-source) 3-D seismograms. I noticed the transformation worked very well, the difference in waveform and the phase shift between 2-D and 3-D seismograms have been corrected. We only have a slight difference in amplitude. Regardless of the distance between source and receiver, the relative percent error remains below 2%.

Chapter 4

Solve the problem of the geometrical spreading using Source time function inversion

4.1 Introduction

In the applied FWI code a 2-D forward solver is implemented. Therefore, line sources are used implicitly in the simulations. However, in general, field data are acquired by hammer blows or explosions which can be approximated by point sources. This causes differences in the wavefields in amplitude and phase. Thus, a point source (3-D) to line source (2-D) transformation must be applied to the field data before the inversion. In the previous chapter, I tested the Validity of the 3-D/2-D transformation which was derived using the Green's functions in 2-D and 3-D dimensions. In this chapter, I tested another 3-D/2-D transformation using the source time function inversion. The aim of the source time function inversion is to reconstruct the source signal used to generate the recorded seismograms. For with the inversion of data recorded in the field, certain parameters in most cases are unknown such as the source signal. Often it can be approximated, or an idealized signal such as the Ricker signal or Fuchs-Müller signal can be used, for example when creating synthetic data. After synthetic data have been computed using a generic source signal, a correction filter can be constructed in such a way that an improved source signal reduces the mismatch to the recorded seismograms. This correction filter is called $source\ wavelet\ correction\ filter$ and was estimated using the method proposed by T. Forbriger and created for full-waveform inversion of field data. In this part of my work, I wanted to simulate 2-D (line source) seismograms using 3-D (point source) seismograms by convolving the 3-D seismograms with the filter wavelet. To illustrate the problem I used the same line source (2-D) seismograms and point source seismograms (3-D) computed in the previous chapter for

homogeneous and reflector models. The seismograms were computed using the numerical FD method.

4.2 Homogeneous model

I used the synthetic 2-D and 3-D seismograms that were introduced in Section 3.4 to test the validity of the source wavelet correction filter derived in the theory part section 2.6. This filter should be able to transform point-source (3-D) seismograms to the corresponding line-source (2-D) seismograms. To generate the seismograms only one source with a center frequency of 40 Hz and one hundred twenty-one receivers located along a straight line were used. Figure 4.1 displayed the 2-D and 3-D seismograms which are normalized to the maximum amplitude of each trace. Not all of the one hundred twenty-one traces are displayed. I selected only twenty traces.

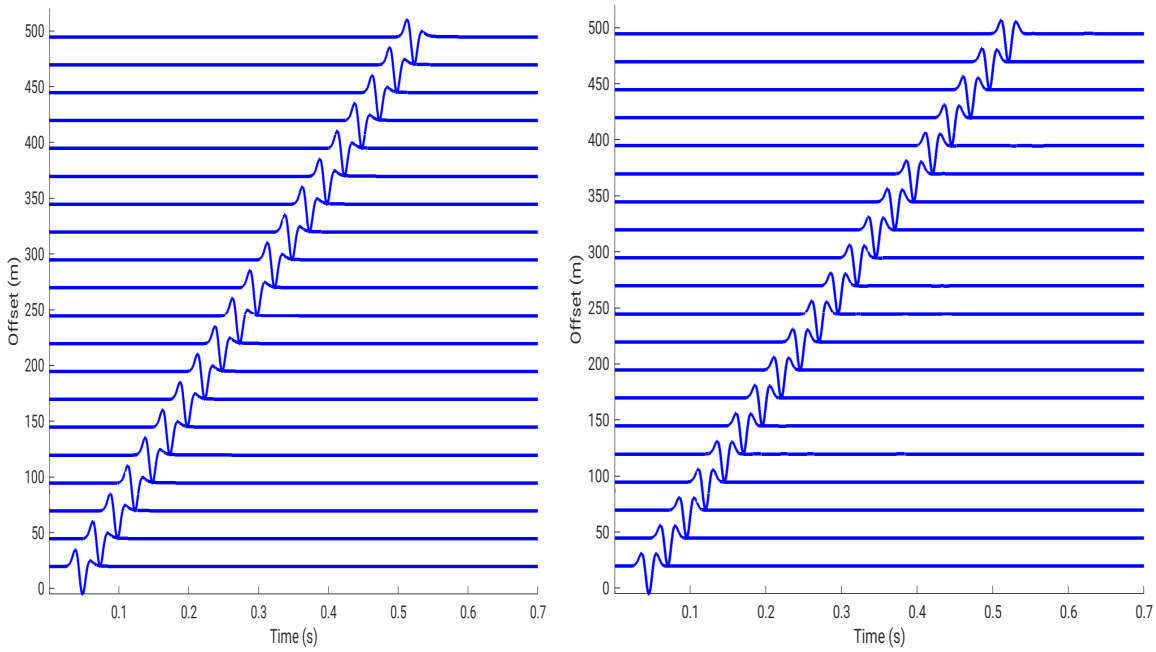

Figure 4.1: Synthetic seismograms generated using the FD method for the homogeneous model. The left plot shows line-source (2-D) seismograms and the right plot shows source-point (3-D) seismograms. The seismograms are normalized to the maximum amplitude of each trace.

The 2-D synthetic seismograms ($g(t)$) of one source at one receiver at position $\vec{x_r}$ was computed with the Green's function of the model m_{2D} via a convolution

$$g(\vec{x_r}, t) = \int_0^T G_{m_{2D}}(\vec{x_s}, \vec{x_r}, t-\tau) s_{2D}(\tau) d\tau, \tag{4.1}$$

that corresponds to a multiplication in frequency domain:

$$\tilde{g} = \tilde{G}_{m_{2D}} \tilde{s}_{2D} \tag{4.2}$$

where $\tilde{g}$, $\tilde{G}_{m_{2D}}$ and $\tilde{s}_{2D}$ are the fourier transforms of $g(\vec{x_r}, t)$, $G_{m_{2D}}$ and s_{2D}(t), respectively. The 3-D seismograms ($d(t)$) were calculated in the same way:

$$d(\vec{x_r}, t) = \int_0^T G_{m_{3D}}(\vec{x_s}, \vec{x_r}, t - \tau) s_{3D}(\tau) d\tau. \tag{4.3}$$

In frequency domain, it becomes

$$\tilde{d} = \tilde{G}_{m_{3D}} \tilde{s}_{3D}, \tag{4.4}$$

where $\tilde{d}$, $\tilde{G}_{m_{3D}}$ and $\tilde{s}_{3D}$ are the fourier transforms of $g(\vec{x_r}, t)$, $G_{m_{3D}}$ and s_{3D}(t), respectively. The source wavelet correction filter $\tilde{c}$ in frequency domain should minimize the difference between 3-D and 2-D seismograms so that

$$\tilde{c}\tilde{d} \approx \tilde{g}. \tag{4.5}$$

Because the wavelet filter was calculated in the frequency domain, the entire wavefield was first transformed by converting all the seismograms (3-D) to the frequency domain and then I applied the filter to the data. After that I went back to the time domain to compare the 3-D to 2-D transformed seismograms with the 2D seismograms. Due to the amplitude decay with offset to the source, signals from receivers at larger offset would contribute less to the optimization criterion for which the source wavelet correction filter is constructed (Forbriger, 2015). Instead of using the scaling coefficient $f_k = (\frac{r_{0_k}}{1m})^{\alpha}$, I normalized all the seismograms to the maximum of each trace to ensure that all receivers, independently of their offset, contribute to an equal average amount to the least-squares objective function in equation 2.65 (Groos, 2014).

I first applied the wavelet filter on the 3-D (point source) seismograms without normalizing the traces to see how well the filter should work. Figure (4.4) displays the results after applying the 3-D/2-D transformation using the source time function inversion. The seismograms are not trace normalized. I selected six traces in the near, mid, and far offset for a better view (see Figure (4.3). I noticed that for the seismogram where the source and receiver are at the same location (offset= 0 m), the transformation works very well: the phase shift between 2-D and 3-D wavefield was corrected, and the waveform fit perfectly too, only a very slight difference in amplitude was observed. For other recorded seismograms, especially for that at the offset equal to 5 m, which corresponds to the position of the second receiver, I noticed that the phase shift and the waveform were well corrected but the amplitude decay with the offset was not corrected. For traces with offset greater than 5 m, the same observation is made.

In Figure 4.4, the 3-D/2-D transformation using the source time function inversion is displayed. But in this case, the seismograms are normalized to the maximum of each trace. I also selected six traces in the near, mid, and far offset for better visibility (see Figure (4.5)). I noticed that for the trace at the offset equal to 0 m the wavelet filter did not work very well, although the waveform was corrected perfectly, there was a difference in amplitude and the phase. For the trace recorded at the offset of 5 m, I noticed that the correction worked well, the corrected seismogram fit well with the 2-D seismogram, and I only noticed a slight difference in amplitude. For the other four seismograms recorded in the mid and far offset, the source wavelet filter worked perfectly well: the 3-D to 2-D seismograms matched perfectly with the 2-D seismograms.
To quantify the difference between 2-D seismograms $data2D$ and the 3-D-to-2-D corrected seismograms $data3D_{corrected}$, I computed the L2 norm with the formula:

$$E = \frac{\sum_{l=0}^{N}(data2D - data3D_{corrected})^2}{\sum_{l=0}^{N} data2D^2}. \tag{4.6}$$

The result can be seen in Figure 4.6. I noticed that the relative errors for the source wavelet correction filter, after the seismograms were normalized, decreased with offsets from 11.5 $\%$ to about 0.1 $\%$ for offsets between 0 m and 10 m approximately. Above these offsets, the curve remains almost constant with an error below 0.1%.

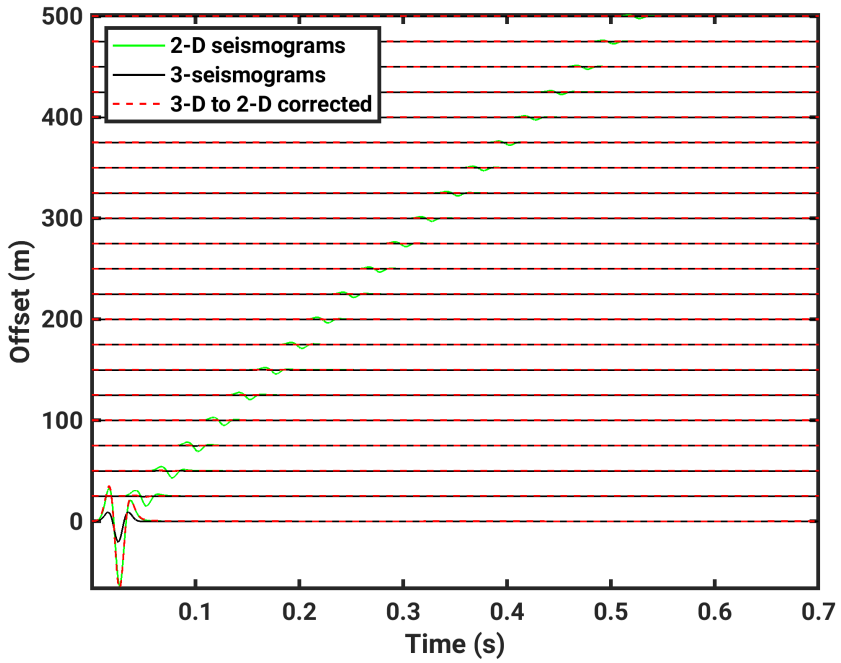

Figure 4.2: Synthetic 2D (blue line) and Synthetic 3D (black line) seismograms were generated using the FD method. 3D-to-2D transformed seismograms (dashed red line) were obtained using the source time function inversion. The seismograms are not normalized to the maximum of each trace.

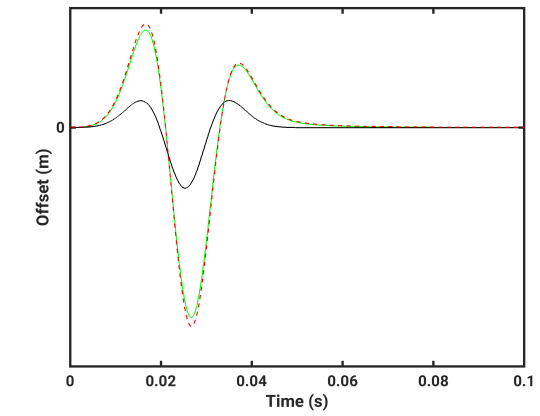

(a) Seismogram recorded at offset 0 m

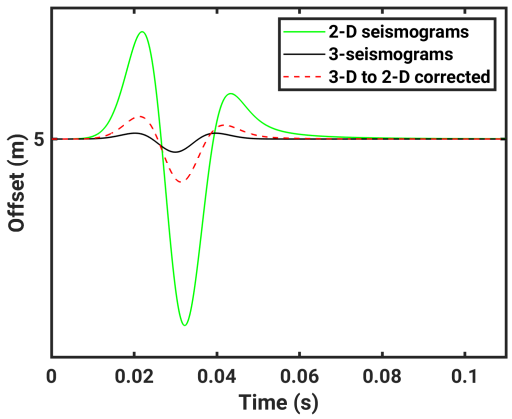

(b) Seismogram recorded at offset 5 m

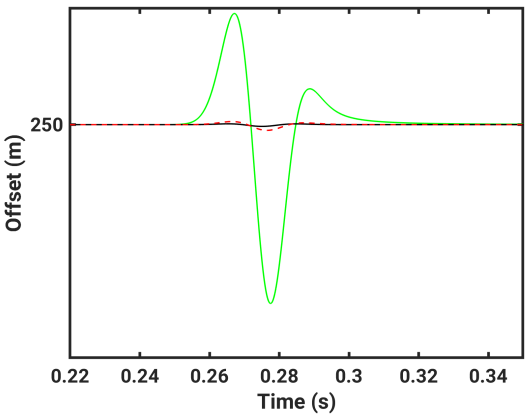

(c) Seismogram recorded at offset 250 m

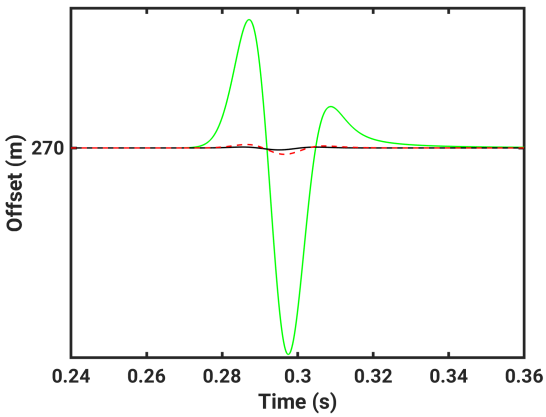

(d) Seismogram recorded at offset 270 m

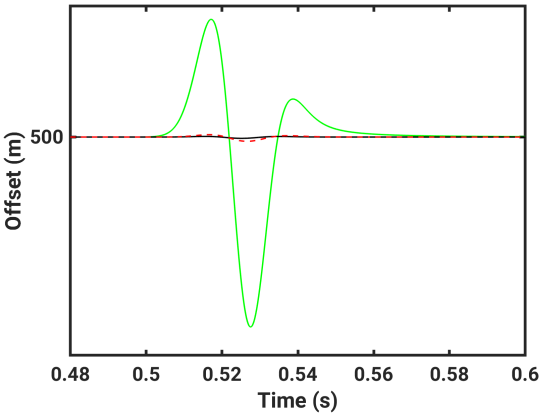

(e) Seismogram recorded at offset 500 m

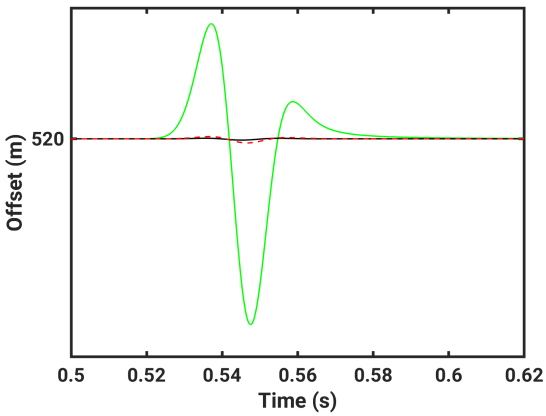

(f) Seismogram recorded at offset 520 m

Figure 4.3: Seismograms comparisons at different source-receivers distance. Synthetic 2D (blue line) and Synthetic 3D (black line) seismograms were generated using the FD method. 3D-to-2D transformed seismograms (dashed red line) were obtained using the source time function inversion. The seismograms were normalized to the maximum of each trace.

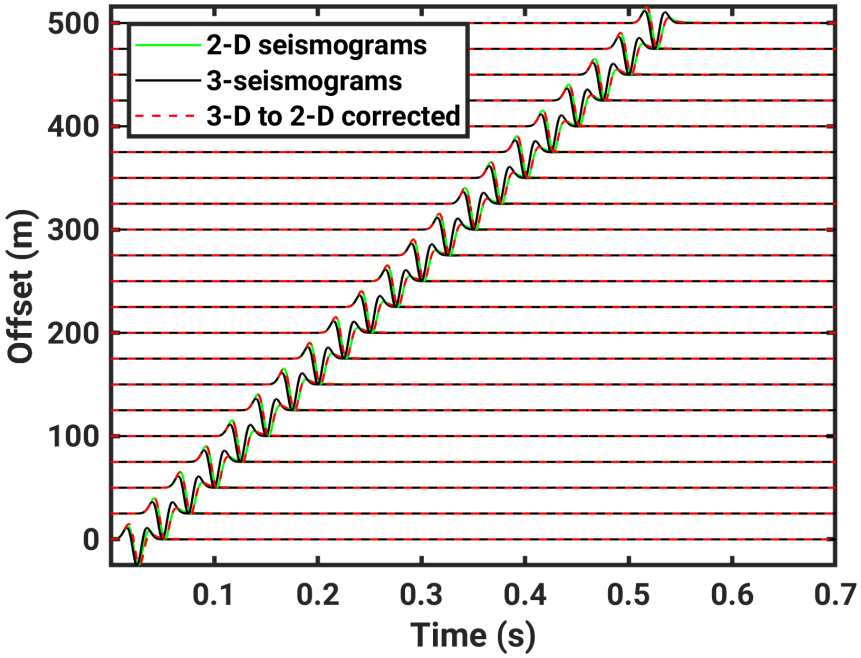

Figure 4.4: Synthetic 2D (blue line) and Synthetic 3D (black line) seismograms were generated using the FD method. 3D-to-2D transformed seismograms (dashed red line) were obtained using the source time function inversion. The seismograms were normalized to the maximum of each trace.

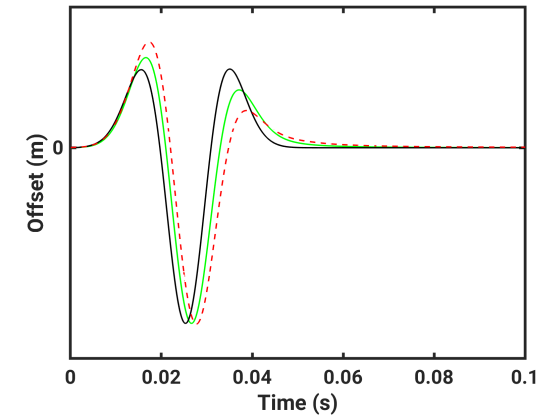

(a) Seismogram recorded at offset 0 m

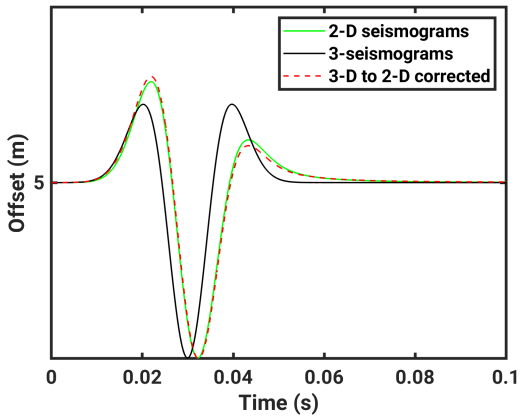

(b) Seismogram recorded at offset 5 m

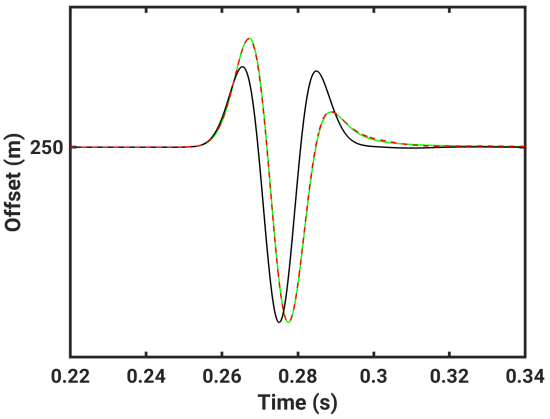

(c) Seismogram recorded at offset 250 m

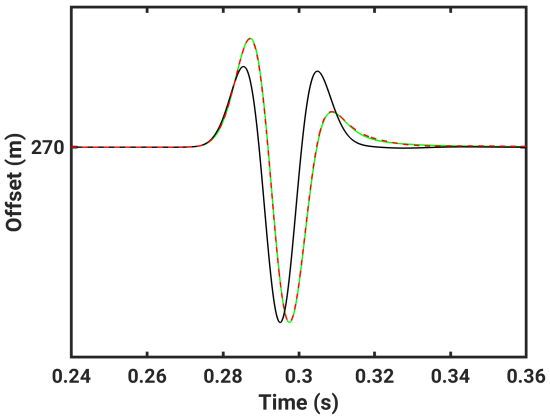

(d) Seismogram recorded at offset 270 m

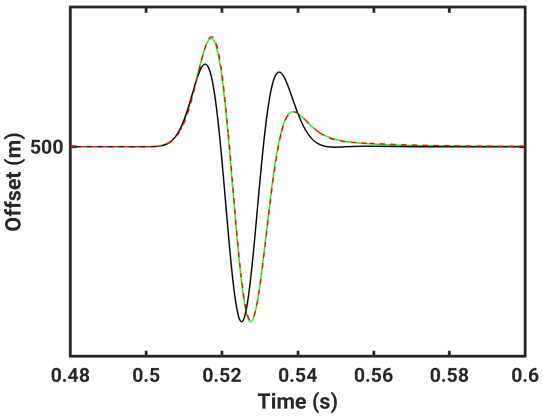

(e) Seismogram recorded at offset 500 m

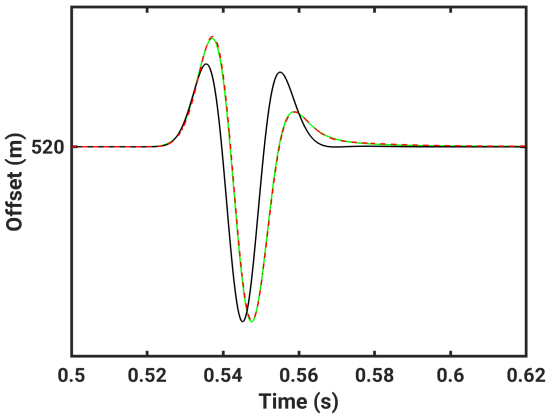

(f) Seismogram recorded at offset 520 m

Figure 4.5: Seismograms comparisons at different source-receivers distance. Synthetic 2D (blue line) and Synthetic 3D (black line) seismograms were generated using the FD method. 3D-to-2D transformed seismograms (dashed red line) were obtained using the source time function inversion. The seismograms were normalized to the maximum of each trace.

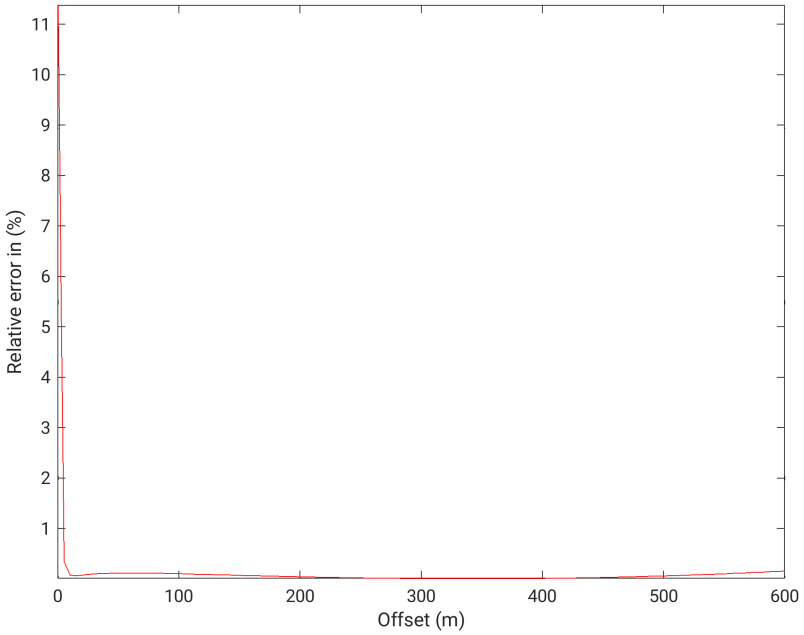

Figure 4.6: Relative errors as a function of offset for the source wavelet correction filter applied on point-source seismograms computed using the numerical FD method for the homogeneous model.

4.3 Reflector model

The seismograms that were used to test the validity of the source wavelet correction filter for reflected waves were the same that I used in section 3.5. These seismograms were generated using an explosive source located inside the model and recorded by one hundred twenty-one receivers which are located on the right-hand side of the source with a spacing interval of 5 m. Figure 4.7 displayed the 2-D and 3-D seismograms which are normalized to the maximum amplitude of each trace. Not all of the one hundred twenty-one traces are displayed. I selected only twenty traces.

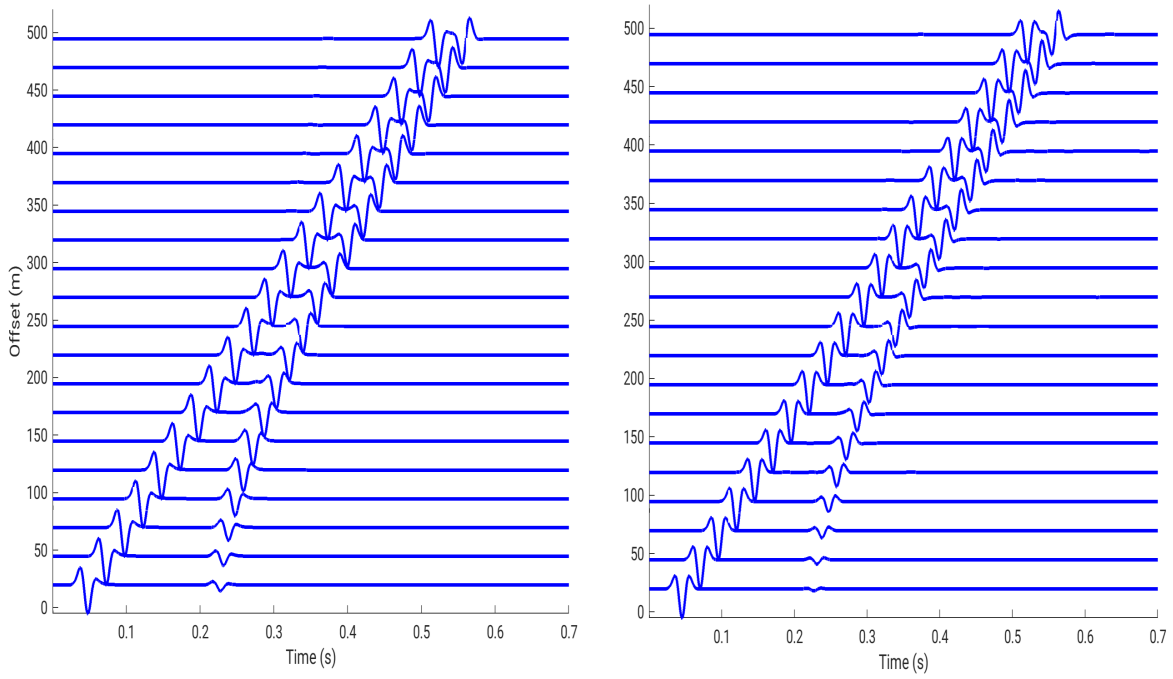

Figure 4.7: Synthetic seismograms generated using the FD method for a reflector model. The left plot shows line-source (2-D) seismograms and the right plot shows source-point (3-D) seismograms. The seismograms were normalized to the maximum amplitude of each trace.

On the seismograms, two different types of waves are seen namely direct waves and reflected waves. I first tested the wavelet filter on (3-D) seismograms without separating the wave types. The results can be seen in Figure (4.8. Only a selection of representative traces(six) of the near, middle, and far offsets are shown. I noticed that when the trace was at the offset equal to 0 m (source and receiver are at the same position), the transformation worked quite well for the direct wave: waveform and phase shift were well corrected but the amplitude was not well corrected. Moreover, I noticed that the amplitude of the corrected seismogram was greater than that of the 2D seismogram. In the case of the reflected wave, the transformation was bad. The same remark was made for the trace at the offset equal to 5 m. For traces at middle offsets (between 250 m and 270 m), I noticed that the transformation worked well for direct waves (waveform, phase shift, and amplitude were well corrected). For the reflected

waves the transformation also worked well, I noticed a slight difference in amplitude. For traces at far offsets (between 500 m and 520 m) the transformation worked very well for both direct waves and reflected waves. Furthermore, to quantify the result, the L2norm was calculated, and the curve with respect to the offset can be observed in Figure 4.9. The curve decreased from about 12 % to 1.5 % for offsets between 0 m and 5 m. Then between 5 m and 100 m, the curve increased until 3 % and from 100 m to 600 m the error continuously decreased from 3 % to approx. 0 %.

Next, I tested the wavelet filter only on the reflected waves to transform the point source seismograms into line source seismograms. The seismograms with only reflected waves can be seen in Figure 4.10. After applying the correction filter on the point source seismograms I selected only six traces in the near, mid, and far offsets for a better view (see Figure 4.11). In general, I noticed that the 3-D/2-D corrected seismograms fit very well with the 2-D (line source) seismograms. The waveform and phase difference between the point source and line source seismograms were perfectly corrected. Only a very small difference in amplitude could be observed. Also noteworthy is that for certain traces, the amplitude of the 3-D/2-D corrected seismograms were greater than that for 2-D seismograms and vice versa. The quantitative result can be seen in Figure 4.12. Although the curve representing the relative error with respect to offsets was not constant (it went up and down), the relative error for all offsets remained below 1.1 %.

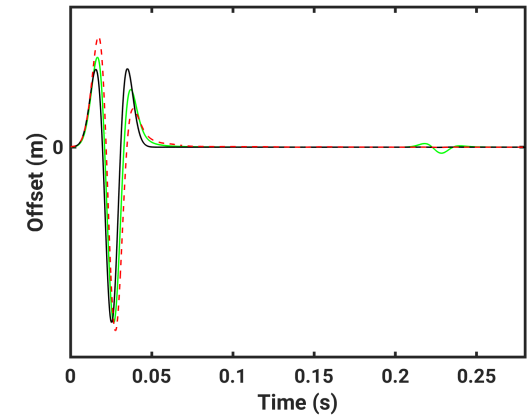

(a) Seismogram recorded at offset 0 m

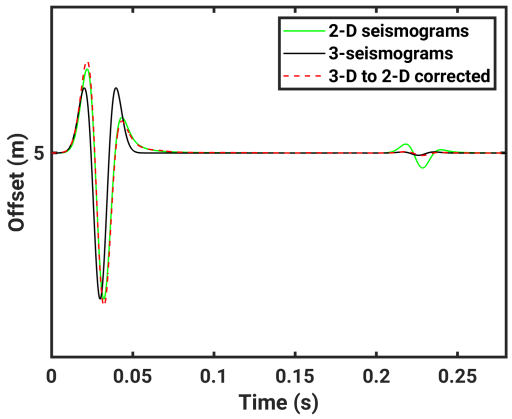

(b) Seismogram recorded at offset 5 m

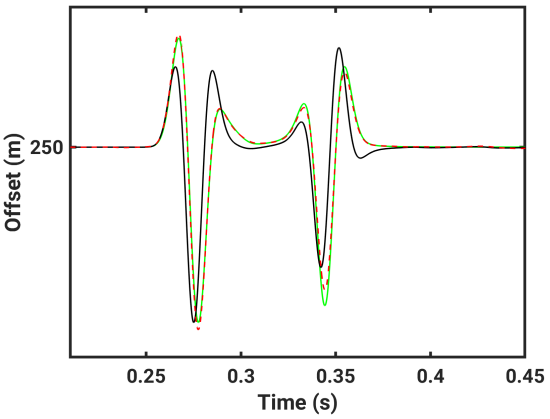

(c) Seismogram recorded at offset 250 m

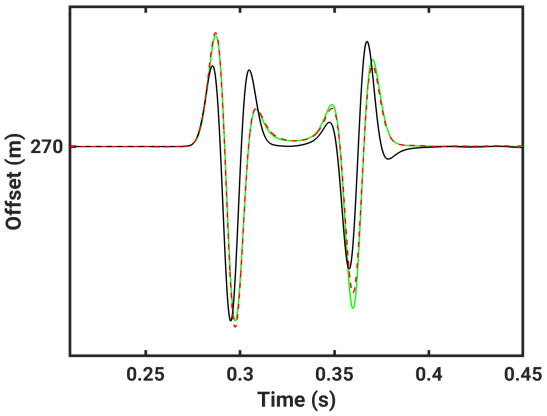

(d) Seismogram recorded at offset 270 m

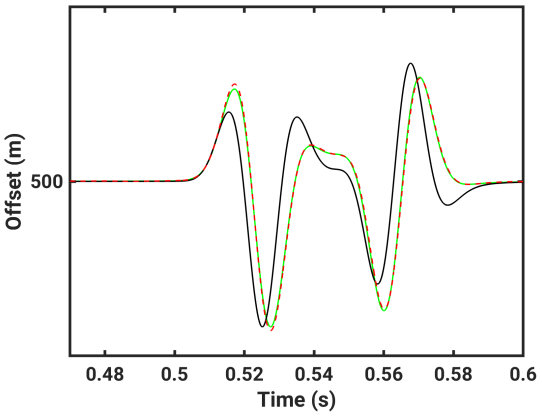

(e) Seismogram recorded at offset 500m

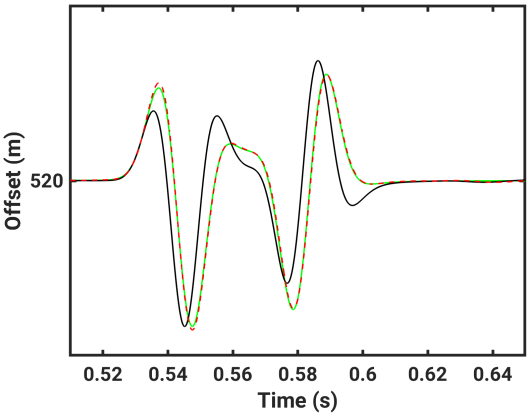

(f) Seismogram recorded at offset 520 m

Figure 4.8: Seismograms comparisons at different source-receivers distance. Synthetic 2D (blue line) and Synthetic 3D (black line) seismograms were generated using the FD method. 3D-to-2D transformed seismograms (dashed red line) were obtained using the source time function inversion. The seismograms were normalized to the maximum of each trace.

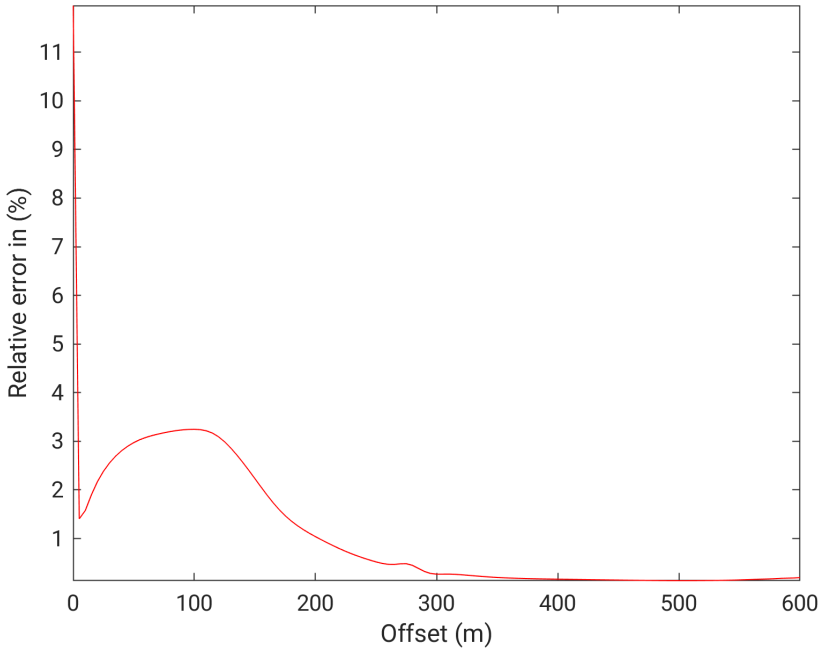

Figure 4.9: Relative errors as a function of offset for the source wavelet correction filter applied on point-source seismograms computed using the numerical FD method for the reflector model. The wavelet filter was applied to the seismograms that contain direct waves and reflected waves.

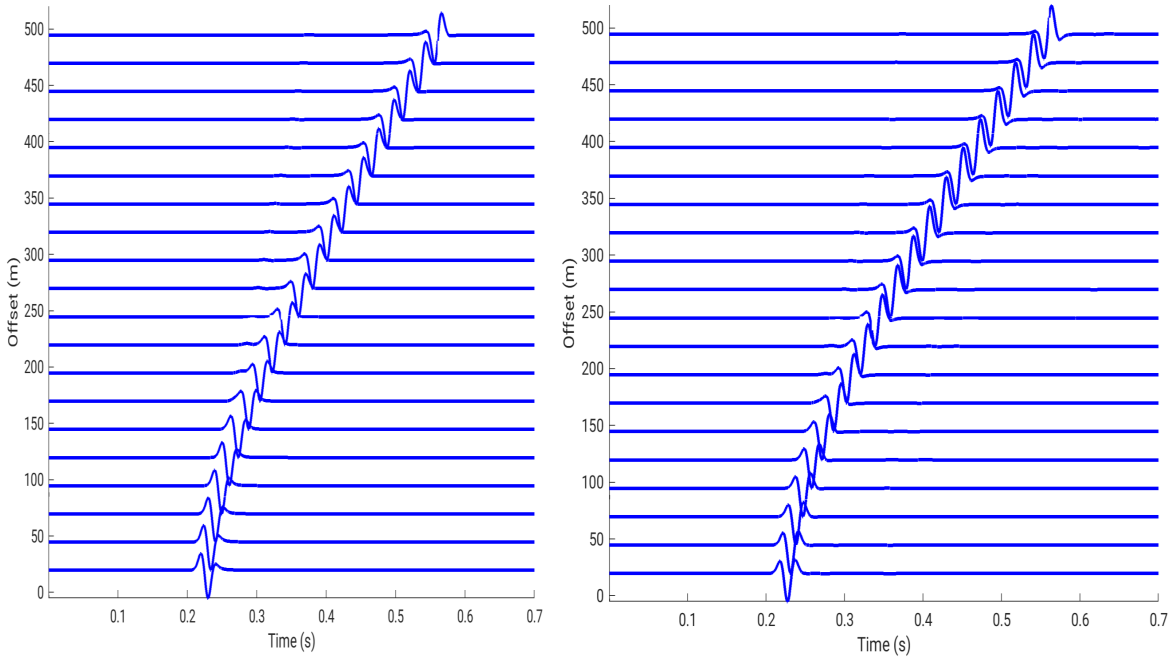

Figure 4.10: Synthetic seismograms generated using the FD method for a reflector model. The left plot shows line-source (2-D) seismograms and the right plot shows source-point (3-D) seismograms. The seismograms were normalized to the maximum amplitude of each trace.

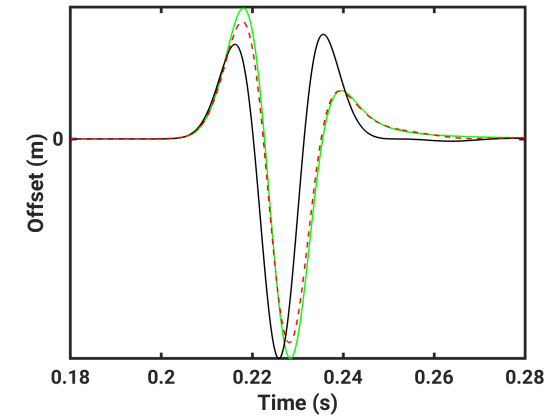

(a) Seismogram recorded at offset 0 m

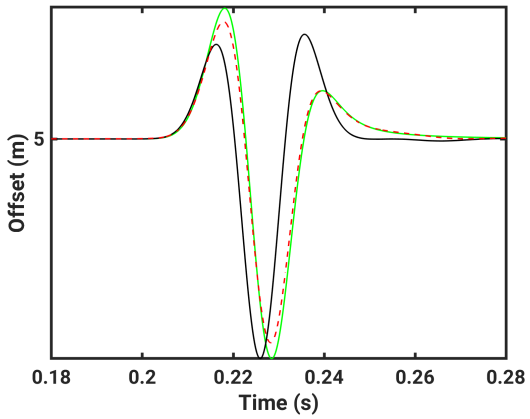

(b) Seismogram recorded at offset 5 m

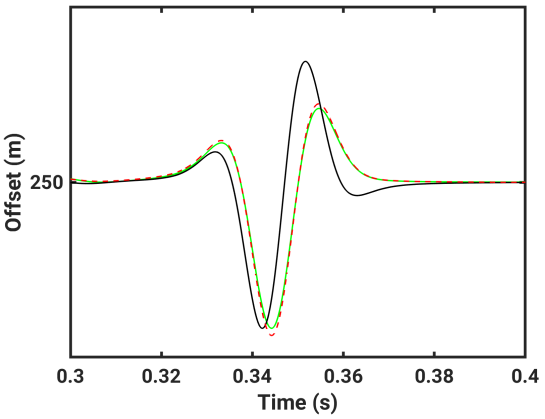

(c) Seismogram recorded at offset 250 m

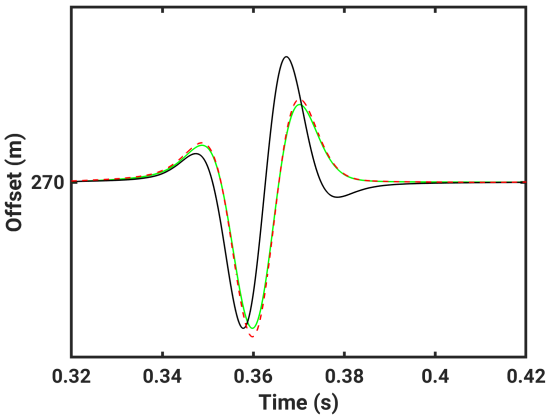

(d) Seismogram recorded at offset 270 m

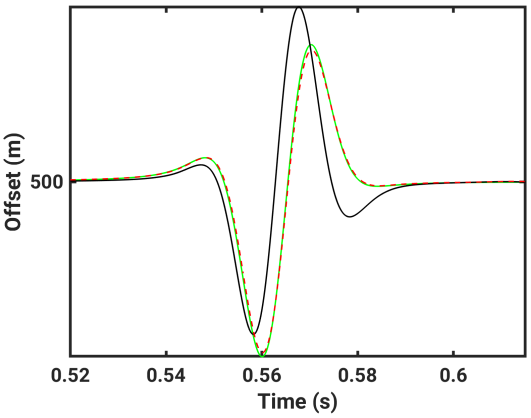

(e) Seismogram recorded at offset 500 m

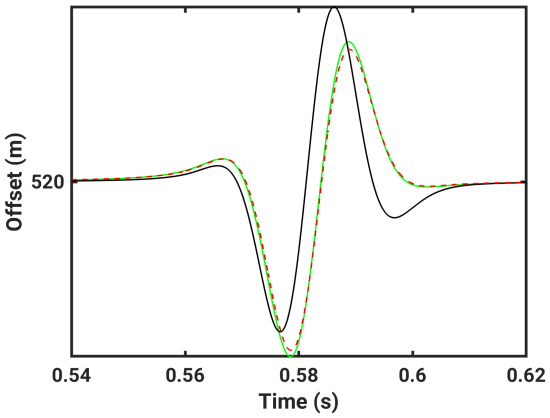

(f) Seismogram recorded at offset 520 m

Figure 4.11: Seismograms comparisons at different source-receiver distances. Synthetic 2-D (blue line) and Synthetic 3-D (black line) seismograms were generated using the FD method. 3-D-to-2-D transformed seismograms (dashed red line) were obtained using the source time function inversion. The seismograms were normalized to the maximum of each trace.

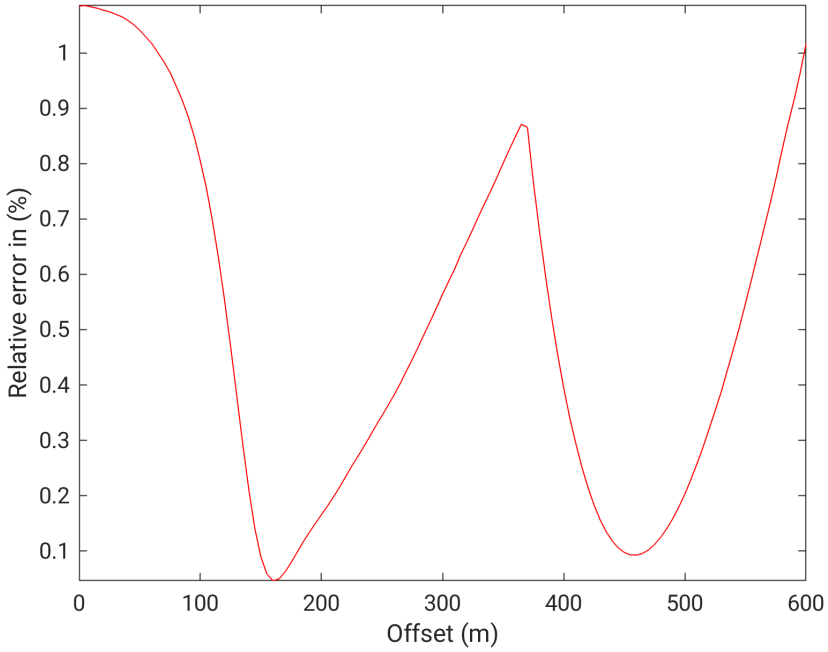

Figure 4.12: Relative errors as a function of offset for the source wavelet correction filter. applied on point-source seismograms computed using the numerical FD method for the reflector model. The wavelet filter was applied on the seismograms that contain only reflected waves.

4.4 Sumarize and discusion

In this chapter, I evaluated the accuracy of the 3-D/2-D transformation using the source wavelet correction filter estimated using the method proposed by T. Forbriger. This transformation was tested on 3-D (point source) seismograms with the purpose of obtaining similar 2-D (line source) seismograms. Two models were used namely homogeneous and reflector model with two layers. The synthetic 2-D and 3-D seismograms were calculated using the numerical FD method.

4.4.1 Homogenous model

In this part, the 3-D/2-D transformation was tested on direct waves. I tested first the transformation by convolving the wavelet filter with the 3-D seismograms that were not normalized. Only for the first trace, where the source and the receiver are at the same location: offset equal 0 m, the 2-D seismograms and the corrected seismograms fitted very well in phase, waveform, and amplitude. For other traces recorded at different offsets, only the amplitude difference between 3-D and 2-D was not corrected. In general, this transformation is bad when the seismograms are not normalized.
To suppress the difference in the amplitude decay with offset, the seismograms were normalized to the maximum amplitude of each trace. A better result could be observed except for the first trace where a small difference in amplitude was noticed. The relative error with respect to the offset was calculated to quantify the result. From the offset equal to 5 m (receiver position two) to the offset equal to 600 m (last receiver position), this error remains under 0.1 $\%$ which is an excellent result.

4.4.2 reflector model

The seismograms generated for the reflector model contained two different waves: direct waves and reflected waves. I applied the transformation to the whole 3-D seismograms without separating direct waves from reflected waves. The seismograms were normalized. It can be seen that for the near offsets, the correction filter worked quite well for the direct wave and was bad for the reflected waves. With increasing offsets, I noticed that the correction filter for both types of waves was getting better and better. The 3-D/2-D corrected seismograms fitted well with the 2-D seismograms. The relative error decreased from 11% in the near offsets to about 0.1% in the far offsets. After that, the correction filter was applied only to reflected waves. In the near offsets, it can be seen that the filter worked very well on the reflected wave in this case compared to the previous case where the waves were not separated. The relative error for all offsets remained below 1.1 $\%$ which is a very good result.

Chapter 5

Comparison Between the 3-D/2-D transformation derived from the Green's Functions and the 3-D/2-D transformation using the source time function inversion.

In Chapters Three and Four, I used two different methods to transform the point source seismograms into the line source seismograms for the application of FWI. In the first method, I used the geometrical spreading correction filter $F(r,\omega)$ derived in the frequency domain from the 2-D and 3-D Green's functions. In the second method, a linear filter calculated in the frequency domain and called the source wavelet correction filter $C(\omega)$ was used. this linear filter can be defined as stabilized deconvolution of the point source seismograms with the line source seismograms similar to the method proposed by (Pratt, 1999).
the geometrical spreading correction filter F given by

$$F(r,\omega) = \underbrace{\sqrt{2rc}}_{F_{amp}} \underbrace{\sqrt{\frac{\pi}{\omega}} e^{-i\pi/4}}_{\tilde{F}_{\sqrt{t^{-1}}}}$$

is composed of two factors: $amplitude\ correction$ and $phase\ correction$. The amplitude factor, which depends on the travel path r, is designed to correct the difference in amplitude between point source and line source seismograms. Because for the line source, an amplitude decay of $\frac{1}{\sqrt{r_0}}$ by a receiver at a distance r_0 is observed. For the point source the amplitude decays with $\frac{1}{r_0}$. The dependence of the travel path leads to different practical implimentations of amplitude correction, because the travel path differs according to the type of wave. The

phase factor, on the other hand, is independent of the propagation distance but depends on the frequency. Its purposes is to correct the phase differences between the point source seismograms and line source seismograms. In the time domain, this filter depends on the time t and on travel path r.
The Fourier coefficents of second filter that was used to transform the point source to line source seismograms is given by

$$C_l = \frac{\sum_{k=1}^{M} f_k^2 \tilde{g}_{kl}^* \tilde{d}_{kl}}{M\tilde{E}\epsilon^2 + \sum_{k=1}^{M} f_k^2 |\tilde{g}_{kl}|^2},$$

where d_{lk}, g_{lk}, and M represent the point source seismograms, the line source seismograms, and the number of receivers, respectively (Groos, 2014). The scaling factor f_k, given in the equation, which depend on the offset r_0 and is used to compensate the decrease in signal amplitude, was not used in this works. Instead of that, the seismograms was normalized to the maximum amplitude of each trace. The source wavelet correction filter does not depend on the travel part, but only on the time t.

5.1 Methods comparison

5.1.1 Homogeneous model: 3-D/2-D transformations on direct waves

To compare both methods, I considered the relative error. The seismograms were computed using the numerical FD method. The 3-D seismograms were transformed into the 2-D seismograms using on the one hand, the direct-wave transformation defined in equation 2.54 based on the assumption that the velocity c was unknown but the travel path r, which corresponds to the distance between source receiver, was known, and on the other hand the source wavelet correction filter. The relative error as a function of offset for the direct-wave transformation (left) and for the source time function inversion (right) can be seen in Figure 5.1. It was clearly to see that the source time function inversion provided better results than the direct-wave transformation. For the direct-waves transformation, the error decreased from about 45 $\%$ in the near offsets to about 6 $\%$ in the far offsets. However, for the source time function inversion, the error decreased from around 11 $\%$ in the near offsets to around 0.1 $\%$ in the far offsets. In conclusion, The source time function inversion can solve the problem of geometrical spreading better than the direct-Wave transformation in the case of the homogeneous model.

5.1.2 Reflector model: 3-D/2-D transformations on reflected waves

The point source (3-D) seismograms that contain only the reflected waves were transformed into the line source seismograms (2-D) using the reflected wave transformation defined in

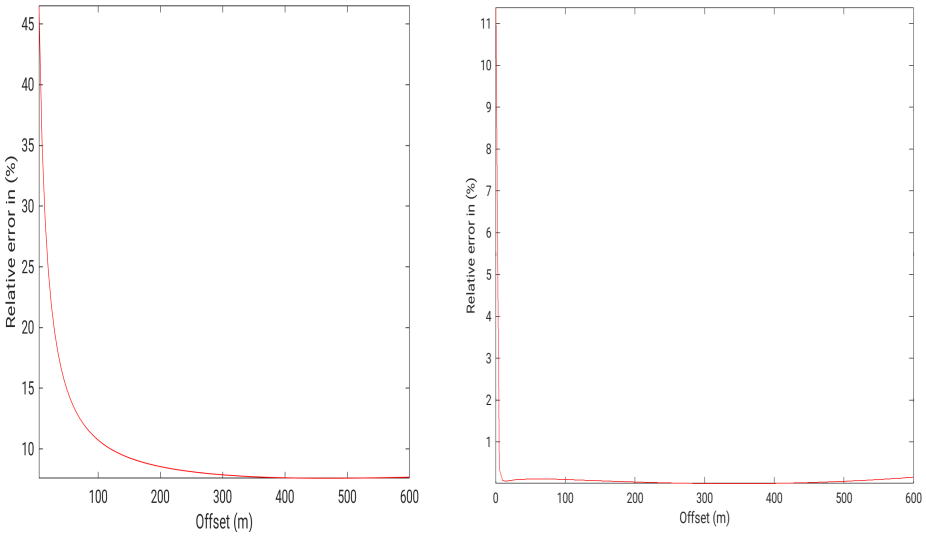

Figure 5.1: Left plot shows the relative errors as a function of offset for the direct-wave transformation and the right plot shows the relative errors as a function of offset for the source wavelet correction filter. The 3-D/2-D transformations were applied to point-source seismograms (contain direct waves) computed using the numerical FD method for the reflector model.

equation 2.51. In this transformation, we made the assumption that the velocity was known, but the travel path was unknown because we did not know the exact location of the reflector. Consequently, the amplitude factor was implemented differently for reflected waves than for direct waves. Because the source wavelet correction filter did not depend on the travel path, The same formula is used for the reflected wave as for the direct wave. Figure 5.2 displayed the relative error as a function of the offset for the reflected wave transformation (left) and for the source time function inversion (right). For both transformations, the relative error for all offsets remains below 1.5 $\%$. But in general, the source time function inversion provides better results than the reflected-wave transformation.

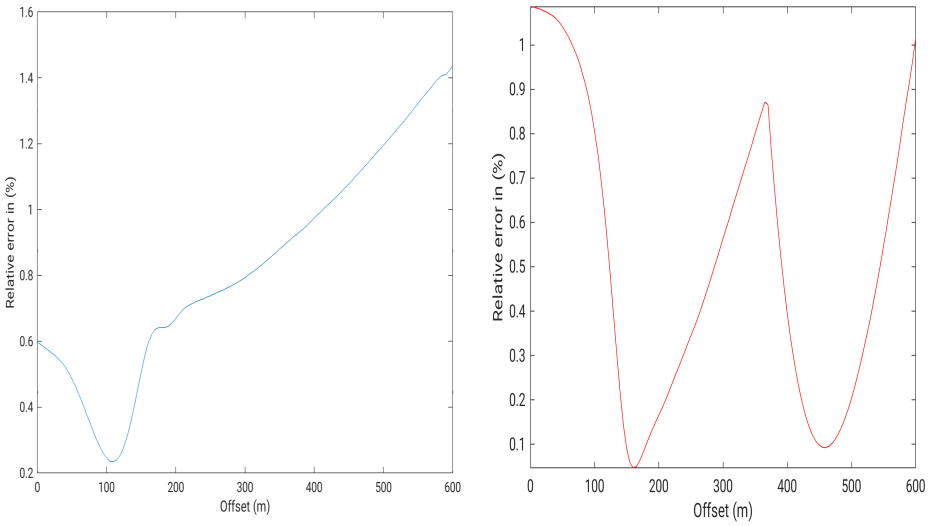

Figure 5.2: Left plot shows the relative errors as a function of offset for the reflected-wave transformation and the right plot shows the relative errors as a function of offset for the source wavelet correction filter. The 3-D/2-D transformations were applied to point-source seismograms (contain only reflected waves) computed using the numerical FD method for the reflector model.

References

Aki, K., & Richards, P. G. (2002). *Quantitative seismology*. University Science Books.

Forbriger, T., Groos, L., & Schäfer, M. (2014). Line-source simulation for shallow-seismic data. part 1: theoretical background. *Geophysical Journal International*, *198*(3), 1387–1404.

Groos, L. (2014). *2d full waveform inversion of shallow seismic rayleigh waves* (Unpublished doctoral dissertation). Karlsruher Instituts für Technologie (KIT).

Lay, T., & Wallace, T. C. (1995). *Modern global seismology*. Elsevier.

Morse, p., & Feshbach, H. (1953). *Methods of theoretical physics*. McGraw-Hill.

Müller, G. (2007). *Theory of elastic waves*. Geoforschungszentrum Potsdam.

Plessix, R.-E. (2006). A review of the adjoint-state method for computing the gradient of a functional with geophysical applications. *Geophysical Journal International*, *167*(2), 495–503.

Pratt, R. G. (1999). Seismic waveform inversion in the frequency domain, part 1: Theory and verification in a physical scale model. *Geophysics*, *64*(3), 888–901.

Schäfer, M., Groos, L., Forbriger, T., & Bohlen, T. (2011). On the effects of geometrical spreading corrections for a 2d fullwaveform inversion of recorded shallowseismic surfacewaves. *Annual WIT report 2011*, *2011*.

Schäfer, M., Groos, L., Forbriger, T., & Bohlen, T. (2012). Testing point source to line source transformations for application of full wave inversion to shallow seismic surface. *Annual WIT report 2012*, *2012*.

Taekhyun, K., Soon, J. S., & Joongmoo, B. (2016). Effective 2d full waveform inversion for 3d seismic data using plane-wave transformation. *Journal of Korean Society of mineral and Energy Resources Engineers*, *2016*.

Tarantola, A. (1984). Inversion of seismic reflection data in the acoustic approximation. *Geophysics*, *49*(8), 1259–1266.

Virieux, J., & Operto, S. (2009). An overview of full-waveform inversion in exploration geophysics. *Geophysics*, *74*(6), WCC1–WCC26.

List of Figures

List of Tables